

# When Anomalies Depend on Context: Learning Conditional Compatibility for Anomaly Detection

Shashank Mishra<sup>1</sup> Didier Stricker<sup>2</sup> Jason Rambach<sup>1</sup>

## Abstract

Anomaly detection is often formulated under the assumption that abnormality is an intrinsic property of an observation, independent of context. This assumption breaks down in many real-world settings, where the same object or action may be normal or anomalous depending on latent contextual factors (e.g., running on a track versus on a highway). We revisit *contextual anomaly detection*, classically defined as context-dependent abnormality, and operationalize it in the visual domain, where anomaly labels depend on subject–context compatibility rather than intrinsic appearance. To enable systematic study of this setting, we introduce CAAD-3K, a benchmark that isolates contextual anomalies by controlling subject identity while varying context. We further propose a conditional compatibility learning framework that leverages vision–language representations to model subject–context relationships under limited supervision. Our method substantially outperforms existing approaches on CAAD-3K and achieves state-of-the-art performance on MVTEC-AD and VisA, demonstrating that modeling context dependence complements traditional structural anomaly detection. Our code and dataset will be publicly released.

## 1. Introduction

Anomaly detection in computer vision is often formulated under the assumption that abnormality is an intrinsic property of an observation: samples that deviate from the distribution of normal data are deemed anomalous, independent of their surrounding context. This assumption underlies most existing vision benchmarks and learning-based methods (Ruff et al., 2018; Chalapathy & Chawla, 2019; Schnei-

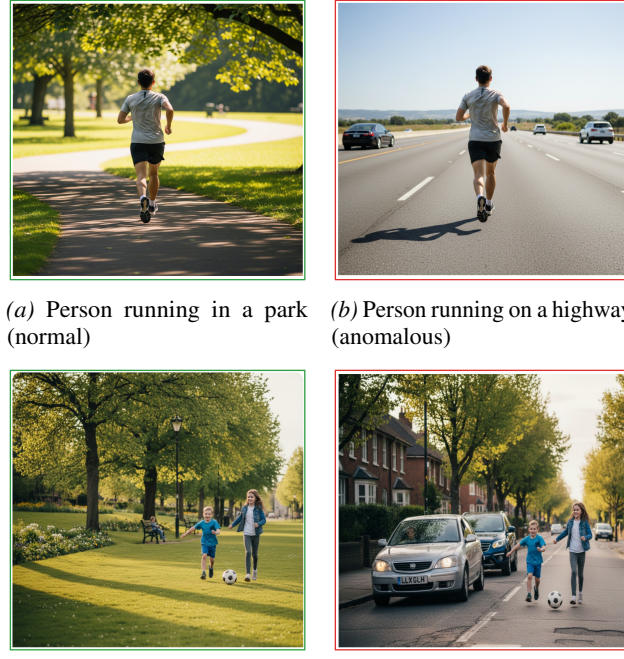


Figure 1. Examples illustrating context-dependent normality. The same action may be normal or anomalous depending on context.

der et al., 2022; Chandola et al., 2009), where anomalies correspond to visual defects, rare patterns, or violations of temporal or semantic consistency. However, in many real-world settings, abnormality is inherently context-dependent. The same object or action may be normal or anomalous depending on its environment, for example, running on a track versus on a highway.

When context is ignored, visually similar observations may admit conflicting anomaly labels, exposing a fundamental limitation of standard anomaly detection. Models trained under intrinsic-label assumptions are incentivized to collapse context-dependent distinctions, making representation learning ill-posed when anomaly labels depend on relationships rather than appearance. Following the classical definition of contextual anomaly detection (Chandola et al., 2009), we consider settings where normality is defined by the compati-

<sup>1</sup>German Research Center for Artificial Intelligence (DFKI)  
<sup>2</sup>Rheinland-Pfälzische Technische Universität Kaiserslautern-Landau (RPTU), Kaiserslautern, Germany. Correspondence to: Shashank Mishra <shashank.mishra@dfki.de>.

bility between a subject and its context rather than intrinsic appearance alone. Unlike structural anomalies, which manifest themselves as appearance outliers, contextual anomalies arise from relational mismatches between otherwise normal entities and their environments.

Despite its prevalence in real-world data and its long-standing recognition in classical anomaly detection, contextual anomaly detection remains underexplored in modern computer vision benchmarks and representation learning settings. Existing benchmarks predominantly encode anomalies as object- or texture-level deviations, making it difficult to evaluate a model’s ability to reason about context-dependent normality. To address this gap, we introduce CAAD-3K, a benchmark explicitly designed to isolate contextual anomalies by holding subject identity constant while varying contextual conditions. CAAD-3K includes a standard split (CAAD-SS) for learning contextual compatibility and a cross-context split (CAAD-CC) that evaluates generalization to unseen subject–context combinations.

To address this setting, we cast anomaly detection as a problem of *conditional compatibility learning*. Under this formulation, a model determines whether a subject is compatible with its surrounding context, rather than whether it deviates from a global notion of normality. We leverage vision–language representations to encode semantic context and design learning objectives that explicitly couple subject and context semantics, enabling context-sensitive discrimination and resolving the non-identifiability inherent in contextual anomaly detection.

Empirically, our model achieves strong performance on CAAD-3K under cross-context generalization and exhibits robust zero-shot transfer to standard anomaly detection benchmarks such as MVTec-AD (Bergmann et al., 2019) and VisA (Zou et al., 2022). Moreover, it attains SOTA results on real-world out-of-context benchmarks, demonstrating effective generalization beyond synthetic settings.

In summary, our contributions are:

- **Problem formulation:** We cast contextual anomaly detection as a conditional compatibility learning problem beyond prior object–context classification formulations.
- **Benchmark and evaluation protocol:** We introduce CAAD-3K, a controlled benchmark with a dedicated cross-context split designed to evaluate generalization under context-dependent labels.
- **Model and learning framework:** We propose CoRe-CLIP, a vision–language framework for conditional compatibility reasoning that achieves state-of-the-art performance on CAAD-3K and other standard anomaly detection benchmarks.

## 2. From Intrinsic to Contextual Anomalies

### 2.1. Contextual Anomaly Detection

In contextual anomaly detection, anomaly labels are *context-dependent* rather than intrinsic. Given an input image  $x \in \mathcal{X}$ , we model latent variables corresponding to a *subject*  $a \in \mathcal{A}$ , which may comprise one or more relevant entities and a surrounding *context*  $c \in \mathcal{C}$ , both entangled in the visual observation. The anomaly label  $y \in \{0, 1\}$  is generated as

$$y = h(a, c), \quad (1)$$

where  $h$  captures the compatibility between subject and context. Consequently, visually similar images may receive different labels under different contexts, violating the common assumption that anomalies can be identified from intrinsic features of  $x$  alone.

### 2.2. Contextual Anomalies in Practice

Figure 1 illustrates the defining characteristic of contextual anomaly detection. In the first example, a person running in a park (Fig. 1a) is considered normal, while the same action performed on a highway (Fig. 1b) is anomalous. In the second example, children playing with a ball in a park (Fig. 1c) is normal, whereas children playing on a residential street (Fig. 1d) constitutes a contextual anomaly.

In all cases, the subject and action are visually similar and individually common; neither the runner nor the children are anomalous in isolation, nor are parks or streets rare scenes. The anomaly arises solely from the incompatibility between the subject and its surrounding context. These examples highlight that contextual anomalies cannot be identified by modeling subjects or scenes independently, but require reasoning about their relationship.

### 2.3. Relation to Existing OOC Settings



(a) Elephant in the room, MIT-OOC (Choi et al., 2012). (b) Cut-Paste OOD setting of COCO-OOC (Acharya et al., 2022).

Figure 2. Examples illustrating context-dependent normality using samples from existing OOC datasets.

Contextual anomaly detection, as considered in this work, differs in important ways from object-centric out-of-distribution (OOD) benchmarks such as MIT-OOC (Choi

et al., 2012) and COCO-OOC (Acharya et al., 2022), examples of which are shown in Fig. 2. In these datasets, anomalies are introduced by placing objects into novel scenes in ways that often induce strong visual or statistical inconsistencies (e.g., implausible scale, geometry, or appearance). Importantly, the semantic label of the object remains intrinsic and invariant to context, while the background primarily induces distributional shift.

From a representation learning perspective, such anomalies can often be addressed using appearance-based or density-based criteria, without requiring explicit subject–context reasoning. In contrast, contextual anomaly detection in CAAD-3K removes these shortcuts by requiring discrimination between visually plausible subject–context combinations, where both components are individually common, and anomalies arise solely from their incompatibility.

#### 2.4. Learning Requirements

This task setting suggests that effective contextual anomaly detection methods should satisfy:

- **Relational reasoning.** The model should assess subject–context *compatibility*, which requires representing subject and context separately rather than relying on a single global embedding.
- **Context-sensitive discrimination.** Predictions should change when context changes while the subject remains fixed, encouraging explicit separation of compatible and incompatible subject–context pairs.
- **Cross-context generalization.** The model should transfer to unseen subject–context combinations by learning semantically grounded compatibility cues rather than memorizing specific pairs.

These requirements motivate the learning objectives and representations introduced in the Section 4.1.

### 3. Related Work

**Vision–language anomaly detection.** Recent anomaly detection methods increasingly rely on pretrained vision–language models such as CLIP (Radford et al., 2021) to enable open-vocabulary inference, moving beyond reconstruction-based (Deng & Li, 2022; He et al., 2024) and feature-matching approaches (Defard et al., 2021; Roth et al., 2022). WinCLIP (Jeong et al., 2023) introduces prompt ensembling for zero-shot defect detection, while AnomalyCLIP (Zhou et al., 2023), AdaCLIP (Cao et al., 2024), PromptAD (Li et al., 2024), and IIPAD (Lv et al., 2025) adapt CLIP via prompt learning or feature refinement for few-shot settings. AA-CLIP (Ma et al., 2025) further injects anomaly-aware supervision into the text encoder to

improve semantic separability. Despite strong performance on industrial benchmarks such as MVTec-AD (Bergmann et al., 2019) and VisA (Zou et al., 2022), these methods treat anomaly detection as an object-centric problem, where anomalies correspond to local defects or appearance deviations, rather than violations of object–scene compatibility.

**Contextual anomaly and out-of-context detection.** Prior work on out-of-context (OOC) recognition includes graph-based reasoning models (Bomatter et al., 2021) and foundation-model-based approaches (Roy et al., 2025). Existing OOC datasets such as MIT-OOC (Choi et al., 2012) and COCO-OOC (Acharya et al., 2022) are limited in scale or rely on cut-and-paste synthesis, conflating contextual inconsistency with low-level artifacts. Additionally, these methods focus on image-level classification and do not support few-shot learning or robust generalization across subject–context combinations.

### 4. Conditional Compatibility Learning

#### 4.1. Motivation and Overview

The task formulation in Section 2.1 reveals a fundamental challenge in anomaly detection with context-dependent labels: when anomaly decisions depend on latent subject–context relationships, intrinsic representations of the observation are insufficient. In such settings, visually similar samples may correspond to different anomaly labels under different contexts, leading to ambiguous or non-identifiable predictions when context is marginalized, a limitation shared by representation-learning-based anomaly detection methods

We address this challenge by casting contextual anomaly detection as a problem of *conditional compatibility learning*. Rather than determining whether an observation is globally anomalous, the model evaluates whether a subject is compatible with its surrounding context. This perspective directly aligns with the learning requirements identified in Section 2.4, including relational reasoning, context sensitivity, and generalization to unseen subject–context combinations.

**Proposition 4.1** (Non-identifiability under intrinsic representation collisions). *Let  $a \in \mathcal{A}$  and  $c \in \mathcal{C}$  denote latent subject and context variables, respectively. Let the observation be generated by  $x = g(a, c) \in \mathcal{X}$ , and the ground-truth anomaly label be given by  $y = h(a, c) \in \{0, 1\}$ , where  $h$  encodes subject–context compatibility. Consider an intrinsic representation  $\phi : \mathcal{X} \rightarrow \mathcal{Z}$  and a detector  $f(x) = \psi(\phi(x))$  for some decision function  $\psi : \mathcal{Z} \rightarrow \{0, 1\}$ . If there exist latents  $a \in \mathcal{A}$  and  $c, c' \in \mathcal{C}$  such that*

$$\phi(g(a, c)) = \phi(g(a, c')) \quad \text{but} \quad h(a, c) \neq h(a, c'), \quad (2)$$

*then no such  $f$  can be correct on both inputs  $x = g(a, c)$  and  $x' = g(a, c')$ .*

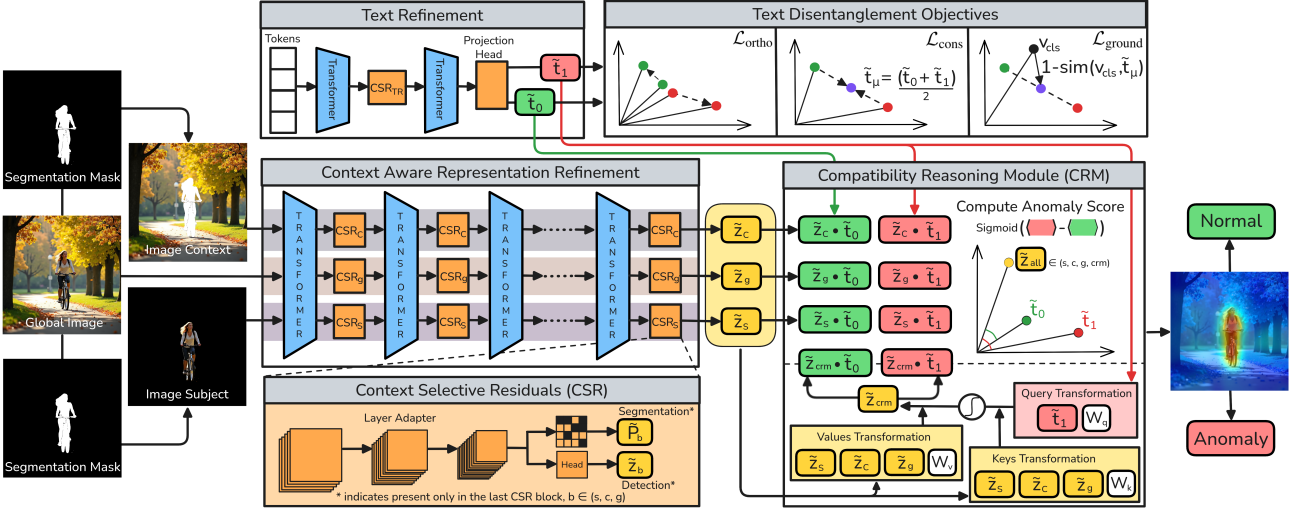


Figure 3. Overview of CoRe-CLIP. A shared CLIP (Radford et al., 2021) backbone is augmented with three **Context-Selective Residual (CSR)** branches for subject, context, and global representations. The refined text encoder, optimized via **Text Disentanglement Objectives**, produces paired normal/anomalous embeddings, while the **Compatibility Reasoning Module (CRM)** fuses the visual streams to infer object–scene compatibility. At inference time, the same input image is passed to all three branches, and no segmentation masks or external region proposals are used.

*Proof Sketch.* The detector  $f$  is a deterministic function of the intrinsic representation  $\phi(x)$ . If two distinct subject–context configurations collapse to the same representation, then  $f(x) = f(x')$  despite requiring different outputs since  $h(a, c) \neq h(a, c')$ . Such representation collisions make contextual anomaly labels non-identifiable from intrinsic information and motivate explicit subject–context modeling.  $\square$

#### 4.2. Representation Decomposition

Proposition 4.1 implies that contextual anomaly detection cannot be addressed using intrinsic representations that entangle subject and context. To enable conditional compatibility reasoning, we therefore decompose each observation into representations that separately capture subject-related and context-related information, while retaining a global view of the scene.

Concretely, given an image  $x$ , we consider three complementary views: a subject-focused representation emphasizing the foreground entity or action, a context-focused representation capturing background or scene information, and a holistic representation of the full image. This decomposition enables explicit reasoning about subject–context relationships, rather than relying on a single marginal embedding that conflates the two.

By maintaining distinct subject and context representations alongside a global view, the model can evaluate whether an otherwise normal subject is compatible with its surrounding context, directly supporting the relational reasoning and context sensitivity requirements in Section 2.4.

## 5. Model Instantiation

### 5.1. Visual and Text Representations

We instantiate conditional compatibility learning in *CoRe-CLIP* Figure 3 using a pretrained vision–language model. Given an input image  $x$ , a shared visual encoder produces embeddings for three complementary views: subject-focused ( $z_s$ ), context-focused ( $z_c$ ), and global ( $z_g$ ).

Textual representations are produced by a trainable text encoder from class descriptions. Visual and textual embeddings are mapped into a shared semantic space, enabling compatibility assessment via cosine similarity.

### 5.2. Context-Aware Representation Refinement

Starting from the visual embeddings  $\{z_s, z_c, z_g\}$  defined above, we refine representations using lightweight, context-aware adaptation modules.

We introduce *Context-Selective Residuals* (CSR), a set of lightweight residual adapters applied independently to subject, context, and global visual features. CSR produces refined embeddings

$$\tilde{z}_s = \text{CSR}_s(z_s), \quad \tilde{z}_c = \text{CSR}_c(z_c), \quad \tilde{z}_g = \text{CSR}_g(z_g).$$

By conditioning residual adaptation on representation type, CSR enhances subject–context relational cues while preserving the pretrained vision–language alignment of the CLIP backbone. Despite receiving the same image at inference, the use of branch-specific CSR adapters induces persistent functional specialization across subject, context, and global pathways.

### 5.3. Text Refinement for Contextual States

Contextual anomaly detection requires text embeddings to represent distinct semantic states of the same concept, corresponding to *contextually normal* and *contextually anomalous* interpretations. To this end, we refine CLIP text representations using a lightweight text adaptation module that produces paired embeddings  $(\tilde{t}_0, \tilde{t}_1)$  for each class or action.

The refined embeddings are optimized using complementary disentanglement objectives: an *orthogonality loss* to separate normal and anomalous interpretations, an *intra-class consistency loss* to preserve shared identity, and an *image–text grounding loss* to maintain alignment with visual semantics.

$$\begin{aligned} \mathcal{L}_{\text{text}} = & \lambda_{\text{ortho}} \langle \tilde{t}_0, \tilde{t}_1 \rangle^2 + \lambda_{\text{cons}} \sum_{k \in \{0,1\}} \|\tilde{t}_k - \tilde{t}_\mu\|_2^2 \\ & + \lambda_{\text{ground}} (1 - \text{sim}(\tilde{t}_\mu, \mathbf{v}_{\text{cls}})), \end{aligned} \quad (3)$$

where  $\tilde{t}_\mu = (\tilde{t}_0 + \tilde{t}_1)/2$  and  $\mathbf{v}_{\text{cls}}$  denotes the visual class token. Full definitions are provided in Appendix A.3.

### 5.4. Compatibility Aggregation and Anomaly Scoring

Contextual anomalies arise from mismatches between subject and context rather than from either component alone. Given refined visual embeddings  $\{\tilde{z}_s, \tilde{z}_c, \tilde{z}_g\}$  and refined text embeddings  $(\tilde{t}_0, \tilde{t}_1)$ , branch-level compatibility scores are insufficient in isolation, as contextual anomalies are inherently relational.

We introduce a *Compatibility Reasoning Module* (CRM) that performs *text-conditioned* aggregation over subject, context, and global representations. CRM infers adaptive weights conditioned on textual semantics and produces a fused representation  $\tilde{z}_{\text{crm}}$  encoding subject–context compatibility. Anomaly scoring is performed by comparing  $\tilde{z}_{\text{crm}}$  with normal and anomalous text embeddings. During training, image-space supervision combines branch-level and fusion-level objectives to supervise CRM reasoning and stabilize attention:

$$\begin{aligned} \mathcal{L}_{\text{img}} = & \sum_{b \in \{s, c, g\}} \text{CE}([\text{sim}(\tilde{z}_b, \tilde{t}_0), \text{sim}(\tilde{z}_b, \tilde{t}_1)], y) \\ & + \text{CE}([\text{sim}(\tilde{z}_{\text{crm}}, \tilde{t}_0), \text{sim}(\tilde{z}_{\text{crm}}, \tilde{t}_1)], y) \\ & + \lambda_{\text{fuse-cons}} \left\| \ell_{\text{crm}} - \frac{1}{3} \sum_b \ell_b \right\|_2^2 + \lambda_{\text{fuse-ent}} (-H(\alpha)). \end{aligned} \quad (4)$$

All embeddings are  $\ell_2$ -normalized,  $\text{sim}(\cdot, \cdot)$  denotes cosine similarity,  $y \in \{0, 1\}$  is the contextual label,  $\ell_b$  and  $\ell_{\text{crm}}$  are branch and fused logits, and  $\alpha$  are CRM attention weights. Cross-entropy supervises branch and fused predictions, while consistency and entropy regularize fusion. Full details in Section A.5.

### 5.5. Training Objective

CoRe-CLIP is trained end-to-end using combined image-space and text-space objectives. Image-space losses enforce subject–context compatibility via branch and CRM fusion supervision, while text-space losses regularize refined textual representations. The overall training objective is:

$$\mathcal{L}_{\text{total}} = \mathcal{L}_{\text{img}} + \mathcal{L}_{\text{text}}, \quad (5)$$

where  $\mathcal{L}_{\text{img}}$  aggregates branch-level and CRM fusion losses, and  $\mathcal{L}_{\text{text}}$  combines orthogonality, consistency, and grounding objectives on the refined text embeddings. Full loss definitions and training details are provided in Section A.8.

## 6. Experiments

### 6.1. Datasets

**CAAD-3K.** We evaluate contextual anomaly detection on CAAD-3K, a benchmark designed to isolate subject–context incompatibility. The dataset contains 3,000 images evenly split between normal and contextual anomaly cases, where anomaly labels are defined by subject–context relationships rather than intrinsic appearance.

CAAD-3K is divided into two subsets. **CAAD-SS** includes 2,095 images for training and in-distribution evaluation, while **CAAD-CC** contains 905 images constructed for cross-context evaluation with unseen subject–context combinations at test time, explicitly testing contextual generalization. Details of dataset construction, generation protocol, annotations, and cross-context splits are provided in the Section D.

**Standard Benchmarks.** We additionally evaluate on established anomaly detection benchmarks. MVTec-AD (Bergmann et al., 2019) and VisA (Zou et al., 2022) primarily capture *structural anomalies* arising from appearance deviations. To assess robustness under out-of-context settings, we consider MIT-OOC (Choi et al., 2012) and COCO-OOC (Acharya et al., 2022), which contain real images where anomalies arise from object–scene mismatches.

### 6.2. Models and Baselines

**Proposed Model.** We evaluate CoRe-CLIP, a conditional compatibility learning framework for context-aware anomaly detection that jointly reasons over subject-focused, context-focused, and global representations. CoRe-CLIP introduces region-aware decomposition as a structural inductive bias to address subject–context compatibility, a capability not modeled by prior CLIP-based detectors. This does not constitute privileged anomaly supervision: region masks are used only to partition representations during training, can be obtained automatically, and are not required at inference. Comparisons therefore reflect architectural capability rather than unequal access to anomaly labels.

Table 1. Comparison with state-of-the-art CLIP-based anomaly detection methods on the CAAD-3K Cross-Context benchmark. Results are reported as Image-AUROC (I) and Pixel-AUROC (P) under few-shot settings. CoRe-CLIP substantially outperforms all baselines, demonstrating robust contextual reasoning. **Best** and **second-best** results are highlighted.

Method	Publication	1-shot		2-shot		4-shot	
		I-AUROC	P-AUROC	I-AUROC	P-AUROC	I-AUROC	P-AUROC
CLIP (Radford et al., 2021)	ICML 2021	38.0	45.5	36.0	44.3	44.3	63.1
CRTNet (Bomatter et al., 2021)	ICCV 2021	58.0	60.5	62.2	63.0	65.5	69.8
WinCLIP (Jeong et al., 2023)	CVPR 2023	64.9	69.5	65.3	65.7	67.2	66.7
AnomalyCLIP (Zhou et al., 2023)	ICLR 2024	76.4	78.9	69.9	81.1	64.5	74.8
AdaCLIP (Cao et al., 2024)	ECCV 2024	59.8	49.3	51.2	45.4	52.0	49.4
PromptAD (Li et al., 2024)	CVPR 2024	60.0	64.0	61.2	63.2	62.5	65.0
AA-CLIP (Ma et al., 2025)	CVPR 2025	55.0	71.1	56.7	76.5	44.1	72.4
IIPAD (Lv et al., 2025)	ICLR 2025	45.0	63.2	48.0	64.5	40.0	65.9
CoRe-CLIP (ours)		<b>85.0</b>	<b>97.2</b>	<b>84.4</b>	<b>97.5</b>	<b>87.3</b>	<b>98.3</b>

**CLIP-based Anomaly Detection.** We compare against state-of-the-art CLIP-based (Ma et al., 2025; Li et al., 2024; Cao et al., 2024) anomaly detection methods that rely on image–text alignment for anomaly scoring. All baselines are evaluated using their official implementations and configurations. Reported results on MVTec-AD and VisA are first reproduced for consistency, and the same settings are then applied to CAAD-3K. Full training and evaluation details are provided in Section A.10.

**Foundation Model-based OOC Detection.** To contextualize performance against prior object–context reasoning approaches, we additionally compare against CRTNet (Bomatter et al., 2021), for which an official implementation is available. CRTNet is trained and evaluated on CAAD-3K using its published configuration, with minimal input-level adaptations required to support the CAAD-3K data format.

### 6.3. Evaluation Metrics

We report Area Under the ROC Curve (AUROC) as the primary evaluation metric. Image-level AUROC (I-AUROC) is used to measure anomaly detection performance and serves as the main metric for CAAD-3K, as the task focuses on identifying subject–context incompatibility. For datasets with pixel-level annotations, we additionally report pixel-level AUROC (P-AUROC) to evaluate localization quality.

### 6.4. Implementation Details

We implement CoRe-CLIP using a pretrained CLIP vision–language backbone (Radford et al., 2021) with a ViT-based visual encoder. All backbone parameters are kept fixed; only the context-aware adaptation modules (CSR), text refinement layers, and the compatibility reasoning module (CRM)

are trained, resulting in a small parameter overhead.

Segmentation masks are used *only during training* to obtain region-specific embeddings, using either dataset-provided masks or automatically generated masks (e.g., SAM (Carion et al., 2025)). At inference time, no segmentation or external models are used: the same input image is passed through all three visual branches, and overhead arises solely from parallel execution within the frozen backbone. All images are resized to a fixed resolution, and optimization is performed using Adam (Kingma & Ba, 2017) with a cosine learning rate schedule. Additional implementation details and hyperparameters are provided in Section B.

### 6.5. Main Results on CAAD-3K

Table 1 reports few-shot anomaly detection performance on CAAD-CC under the standard protocol. Across all shot settings, the proposed method consistently outperforms existing CLIP-based anomaly detection approaches in both image-level and pixel-level AUROC. Methods designed for structural anomaly detection or object-centric reasoning exhibit limited robustness under cross-context evaluation, where subject–context relationships differ between training and testing. While recent CLIP-based methods improve over vanilla CLIP through prompt tuning or adaptation, their performance degrades as contextual variability increases.

In contrast, our approach achieves consistently strong performance across all shot regimes, with substantial gains in image-level AUROC, indicating more reliable detection of contextual inconsistencies under limited supervision. These results validate the effectiveness of conditional compatibility learning and highlight the limitations of appearance-driven anomaly scoring in cross-context settings.

Table 2. Zero-shot I-AUROC and P-AUROC on MVTec-AD (Bergmann et al., 2019) and VisA (Zou et al., 2022). CoRe-CLIP achieves state-of-the-art or competitive performance. **Best** and **second-best** results are highlighted.

Method	Publication	MVTec-AD		VisA	
		I-AUROC	P-AUROC	I-AUROC	P-AUROC
CLIP (Radford et al., 2021)	ICML 2021	86.1	38.4	66.4	46.6
WinCLIP (Jeong et al., 2023)	CVPR 2023	91.8	85.1	78.0	79.6
MVFA-AD (Huang et al., 2024)	CVPR 2024	86.6	84.9	76.5	93.4
AnomalyCLIP (Zhou et al., 2023)	ICCV 2023	90.9	91.1	82.1	<b>95.4</b>
AdaCLIP (Cao et al., 2024)	ECCV 2024	90.0	89.9	84.3	<b>95.5</b>
AA-CLIP (Ma et al., 2025)	CVPR 2025	92.0	91.9	84.6	<b>95.5</b>
CoRe-CLIP (Ours)	-	<b>94.2</b>	<b>92.8</b>	<b>84.9</b>	<b>95.5</b>

## 6.6. Generalization to Standard Benchmarks

We evaluate whether conditional compatibility learning generalizes to standard *structural* anomaly detection benchmarks. Table 2 reports image- and pixel-level AUROC on MVTec-AD (Bergmann et al., 2019) and VisA (Zou et al., 2022), following the AA-CLIP protocol (Ma et al., 2025).

*Zero-shot* evaluation denotes cross-dataset transfer: the model is trained on the full split of one dataset (e.g., VisA) and evaluated directly on the other (e.g., MVTec-AD), and vice versa, without using any image-level supervision from the target dataset. Only class names are provided via text prompts at inference time.

For these texture- and surface-centric benchmarks, CoRe-CLIP automatically reduces to a single-branch configuration, as no contextual decomposition is required; no segmentation masks are used during training or inference.

CoRe-CLIP achieves state-of-the-art performance on MVTec-AD and matches or exceeds top-performing methods on VisA, demonstrating that conditional compatibility learning preserves, and does not compromise structural anomaly detection performance.

## 6.7. Out-of-Context Detection on Real Image Benchmarks

We evaluate CoRe-CLIP on MIT-OOC (Choi et al., 2012) and COCO-OOC (Acharya et al., 2022), which contain natural images where anomalies arise from object–scene incompatibility rather than appearance defects. These benchmarks test whether contextual compatibility learned in our framework transfers to heterogeneous, real-image settings.

CoRe-CLIP is evaluated in a *zero-shot transfer* setting: the model is trained on CAAD-3K and directly applied to MIT-OOC and COCO-OOC without any fine-tuning, support set adaptation, or dataset-specific prompt tuning. In contrast,

Table 3. Out-of-context detection accuracy (%) on MIT-OOC and COCO-OOC.

Method	MIT-OOC	COCO-OOC
COC	73.29	-
GCRN	-	84.85
FM-based Zero-shot	90.82	87.26
CoRe-CLIP (Ours)	<b>95.60</b>	<b>97.20</b>

prior foundation-model-based approaches (Roy et al., 2025) operate purely via prompt engineering on pretrained models without task-specific learning.

As shown in Table 3, CoRe-CLIP substantially outperforms both classical context-reasoning methods, COC and GCRN (Choi et al., 2012; Acharya et al., 2022), and recent foundation-model-based zero-shot baselines (Roy et al., 2025), demonstrating strong generalization of conditional compatibility learning to real-world OOC detection.

## 6.8. Ablation Studies

We analyze the contribution of individual components on CAAD-3K (4-shot, cross-context), keeping the backbone fixed across all variants.

Table 4. Each module: CSR, text refinement, and CRM, contributes complementary gains in contextual reasoning.

CSR	Text	CRM	I-AUROC	P-AUROC
✗	✗	✗	44.3	63.1
✓	✗	✗	72.8	91.4
✓	✓	✗	79.6	95.0
✓	✓	✓	<b>87.3</b>	<b>98.3</b>

**Component Analysis.** Table 4 shows that frozen CLIP features perform poorly under contextual shifts. CSR provides

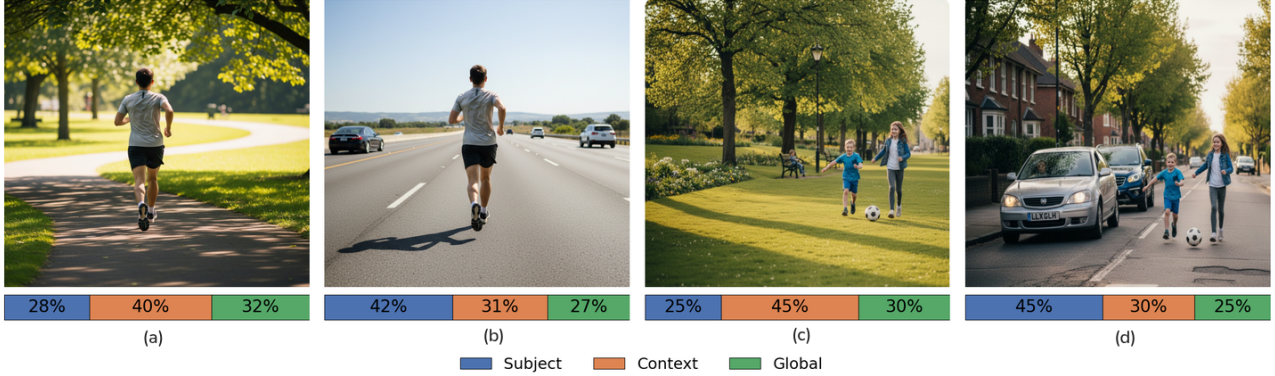


Figure 4. CRM branch weighting for identical actions under normal and anomalous contexts. Bar plots indicate the relative contribution of subject, context, and global representations.

the largest gain, indicating the importance of disentangling subject and context representations. Text refinement further stabilizes semantic alignment, while CRM yields additional improvements by enabling cross-branch reasoning. Together, all components are required for robust contextual anomaly detection.

**Branch Analysis.** As shown in Table 5, using only subject, context, or global cues is insufficient. Only tri-branch fusion achieves strong performance, confirming that contextual anomalies are inherently relational and require joint reasoning over object and scene.

Table 5. Robust object–scene reasoning requires tri-branch fusion; CSR and text losses are active throughout.

Global	Subject	Context	I-AUROC	P-AUROC
✓	✗	✗	67.1	82.4
✗	✓	✗	70.4	87.2
✗	✗	✓	64.2	74.5
✓	✓	✓	<b>87.3</b>	<b>98.3</b>

**Mask Robustness.** Replacing ground-truth masks with automatically generated region proposals (e.g., SAM (Carion et al., 2025)) yields comparable performance, indicating that CoRe-CLIP does not rely on precise manual annotations. Region masks are used only to induce subject- and context-focused representations during training, demonstrating that the framework generalizes to datasets without explicit region annotations. More details in Section A.11.

Table 6. Robustness to absence of gt mask on CAAD-CC.

Mask Source	I-AUROC	P-AUROC
Ground-truth masks	87.3	98.3
SAM-generated masks	85.3	94.5

## 6.9. Qualitative Analysis

As shown in Figure 4, CRM exhibits consistent context-sensitive behavior across different scenarios. For actions/objects placed in compatible scenes (Fig. 4a,c), the model assigns higher weight to context and global representations, reflecting contextual support. When the same actions occur in incompatible environments (Fig. 4b,d), CRM shifts emphasis toward the subject, signaling object–scene mismatch. This redistribution demonstrates that anomaly decisions arise from conditional subject–context reasoning rather than appearance alone.

## 7. Conclusion

We study anomaly detection in a context-dependent setting, where abnormality arises from subject–context incompatibility rather than intrinsic appearance. We formalize this problem as contextual anomaly detection and introduce CAAD-3K, a benchmark that isolates contextual violations by controlling subject identity while varying scene context. To address the resulting non-identifiability of intrinsic representations, we propose CoRe-CLIP, a conditional compatibility learning framework that decomposes visual cues and performs language-conditioned reasoning over subject, context, and global information. Although the individual training objectives are simple, their integration enables context-sensitive compatibility reasoning that is inaccessible to prior anomaly detection models. Extensive experiments show that CoRe-CLIP substantially outperforms existing methods on CAAD-3K while generalizing effectively to standard industrial benchmarks, indicating that context-aware reasoning complements open-vocabulary anomaly detection. More broadly, this work reframes anomaly detection as a relational learning problem and highlights the role of semantic grounding for robust perception in open-world environments; broader scenario coverage is left to future work Section F.

## Impact Statement

This work advances anomaly detection by addressing settings where abnormality depends on subject–context compatibility rather than intrinsic appearance. Modeling such context dependence may improve robustness in perception systems by reducing false positives from context-agnostic detectors. This work advances anomaly detection by addressing settings where abnormality depends on subject–context compatibility rather than intrinsic appearance. Modeling such context dependence may improve robustness in perception systems by reducing false positives from context-agnostic detectors, for example in industrial inspection settings where a visually correct component becomes anomalous when placed in an incompatible location.

The proposed methods are evaluated on a synthetic benchmark and established public datasets and are intended for research use. As the approach relies on pretrained vision–language models, it may inherit biases present in those representations. We do not introduce new real-world data collection or deployment mechanisms, and we do not foresee immediate negative societal impacts; however, responsible downstream use should consider dataset bias and domain-specific validation.

## Acknowledgements

This work was partially supported by the German Federal Ministry of Research, Technology and Space (BMFTR) under Grant Agreement No. 16IW24009 (COPPER).

## References

Acharya, M., Roy, A., Koneripalli, K., Jha, S., Kanan, C., and Divakaran, A. Detecting out-of-context objects using graph context reasoning network. In *IJCAI*, 2022.

Bergmann, P., Fauser, M., Sattlegger, D., and Steger, C. Mvttec ad—a comprehensive real-world dataset for unsupervised anomaly detection. In *Proceedings of the IEEE/CVF conference on computer vision and pattern recognition*, pp. 9592–9600, 2019.

Bomatter, P., Zhang, M., Karev, D., Madan, S., Tseng, C., and Kreiman, G. When pigs fly: Contextual reasoning in synthetic and natural scenes. In *Proceedings of the IEEE/CVF International Conference on Computer Vision*, pp. 255–264, 2021.

Cao, Y., Zhang, J., Frittoli, L., Cheng, Y., Shen, W., and Boracchi, G. Adaclip: Adapting clip with hybrid learnable prompts for zero-shot anomaly detection. In *European Conference on Computer Vision*, pp. 55–72. Springer, 2024.

Carion, N., Gustafson, L., Hu, Y.-T., Debnath, S., Hu, R., Suris, D., Ryali, C., Alwala, K. V., Khedr, H., Huang, A., et al. SAM 3: Segment anything with concepts. *arXiv preprint arXiv:2511.16719*, 2025.

Chalapathy, R. and Chawla, S. Deep learning for anomaly detection: A survey. *arXiv preprint arXiv:1901.03407*, 2019.

Chandola, V., Banerjee, A., and Kumar, V. Anomaly detection: A survey. *ACM computing surveys (CSUR)*, 41(3): 1–58, 2009.

Choi, M. J., Torralba, A., and Willsky, A. S. Context models and out-of-context objects. *Pattern Recognition Letters*, 33(7):853–862, 2012.

Cohen, N. and Hoshen, Y. Sub-image anomaly detection with deep pyramid correspondences. *arXiv preprint arXiv:2005.02357*, 2020.

Defard, T., Setkov, A., Loesch, A., and Audigier, R. Padim: a patch distribution modeling framework for anomaly detection and localization. In *International conference on pattern recognition*, pp. 475–489. Springer, 2021.

Deng, H. and Li, X. Anomaly detection via reverse distillation from one-class embedding. In *Proceedings of the IEEE/CVF conference on computer vision and pattern recognition*, pp. 9737–9746, 2022.

He, H., Zhang, J., Chen, H., Chen, X., Li, Z., Chen, X., Wang, Y., Wang, C., and Xie, L. A diffusion-based framework for multi-class anomaly detection. In *Proceedings of the AAAI conference on artificial intelligence*, volume 38, pp. 8472–8480, 2024.

Huang, C., Jiang, A., Feng, J., Zhang, Y., Wang, X., and Wang, Y. Adapting visual-language models for generalizable anomaly detection in medical images. In *Proceedings of the IEEE/CVF Conference on Computer Vision and Pattern Recognition*, pp. 11375–11385, 2024.

Jeong, J., Zou, Y., Kim, T., Zhang, D., Ravichandran, A., and Dabeer, O. Winclip: Zero-/few-shot anomaly classification and segmentation. In *Proceedings of the IEEE/CVF Conference on Computer Vision and Pattern Recognition*, pp. 19606–19616, 2023.

Jocher, G., Qiu, J., and Chaurasia, A. Ultralytics YOLO, January 2023. URL <https://github.com/ultralytics/ultralytics>.

Kingma, D. P. and Ba, J. Adam: A method for stochastic optimization, 2017. URL <https://arxiv.org/abs/1412.6980>.

Kirillov, A., Mintun, E., Ravi, N., Mao, H., Rolland, C., Gustafson, L., Xiao, T., Whitehead, S., Berg, A. C., Lo, W.-Y., et al. Segment anything. In *Proceedings of the IEEE/CVF international conference on computer vision*, pp. 4015–4026, 2023.

Labs, B. F. Flux.1 [dev]. <https://huggingface.co/black-forest-labs/FLUX.1-dev>, 2025. Accessed: 2025-11-10.

Li, Y., Goodge, A., Liu, F., and Foo, C.-S. Promptad: Zero-shot anomaly detection using text prompts. In *Proceedings of the IEEE/CVF Winter Conference on Applications of Computer Vision*, pp. 1093–1102, 2024.

Liu, S., Zeng, Z., Ren, T., Li, F., Zhang, H., Yang, J., Jiang, Q., Li, C., Yang, J., Su, H., et al. Grounding dino: Marrying DINO with grounded pre-training for open-set object detection. In *European Conference on Computer Vision*, pp. 38–55. Springer, 2024.

Lv, W., Su, Q., and Xu, W. One-for-all few-shot anomaly detection via instance-induced prompt learning. In *The Thirteenth International Conference on Learning Representations*, 2025.

Ma, W., Zhang, X., Yao, Q., Tang, F., Wu, C., Li, Y., Yan, R., Jiang, Z., and Zhou, S. K. Aa-clip: Enhancing zero-shot anomaly detection via anomaly-aware clip. In *Proceedings of the Computer Vision and Pattern Recognition Conference*, pp. 4744–4754, 2025.

Miyai, A., Yang, J., Zhang, J., Ming, Y., Lin, Y., Yu, Q., Irie, G., Joty, S., Li, Y., Li, H., et al. Generalized out-of-distribution detection and beyond in vision language model era: A survey. *arXiv preprint arXiv:2407.21794*, 2024.

OpenAI. GPT-4 technical report. Technical report, OpenAI, 2023. URL <https://cdn.openai.com/papers/gpt-4.pdf>.

Radford, A., Kim, J. W., Hallacy, C., Ramesh, A., Goh, G., Agarwal, S., Sastry, G., Askell, A., Mishkin, P., Clark, J., et al. Learning transferable visual models from natural language supervision. In *International Conference on Machine Learning*, pp. 8748–8763. PMLR, 2021.

Roth, K., Pemula, L., Zepeda, J., Schölkopf, B., Brox, T., and Gehler, P. Towards total recall in industrial anomaly detection. In *Proceedings of the IEEE/CVF conference on computer vision and pattern recognition*, pp. 14318–14328, 2022.

Roy, A., Cobb, A., Kaur, R., Jha, S., Bastian, N. D., Berenbeim, A., Thomson, R., Cruickshank, I., Velasquez, A., and Jha, S. Zero-shot detection of out-of-context objects using foundation models. In *2025 IEEE/CVF Winter Conference on Applications of Computer Vision (WACV)*, pp. 9186–9195. IEEE, 2025.

Ruff, L., Vandermeulen, R., Goernitz, N., Deecke, L., Siddiqui, S. A., Binder, A., Müller, E., and Kloft, M. Deep one-class classification. In *International Conference on Machine Learning*, pp. 4393–4402. PMLR, 2018.

Schneider, P., Rambach, J., Mirbach, B., and Stricker, D. Unsupervised anomaly detection from time-of-flight depth images. In *Proceedings of the IEEE/CVF Conference on Computer Vision and Pattern Recognition*, pp. 231–240, 2022.

Shi, Y., Yang, J., and Qi, Z. Unsupervised anomaly segmentation via deep feature reconstruction. *Neurocomputing*, 424:9–22, February 2021. ISSN 0925-2312. doi: 10.1016/j.neucom.2020.11.018. URL <http://dx.doi.org/10.1016/j.neucom.2020.11.018>.

Yao, X., Zhang, C., Li, R., Sun, J., and Liu, Z. One-for-all: Proposal masked cross-class anomaly detection. In *Proceedings of the AAAI Conference on Artificial Intelligence*, volume 37, pp. 4792–4800, 2023.

You, Z., Yang, K., Luo, W., Cui, L., Zheng, Y., and Le, X. Adtr: Anomaly detection transformer with feature reconstruction. In *International Conference on Neural Information Processing*, pp. 298–310. Springer, 2022.

Zhang, X., Li, S., Li, X., Huang, P., Shan, J., and Chen, T. Destseg: Segmentation guided denoising student-teacher for anomaly detection. In *Proceedings of the IEEE/CVF conference on computer vision and pattern recognition*, pp. 3914–3923, 2023.

Zhou, Q., Pang, G., Tian, Y., He, S., and Chen, J. Anomalyclip: Object-agnostic prompt learning for zero-shot anomaly detection. *arXiv preprint arXiv:2310.18961*, 2023.

Zou, Y., Jeong, J., Pemula, L., Zhang, D., and Dabeer, O. Spot-the-difference self-supervised pre-training for anomaly detection and segmentation. In *European Conference on Computer Vision*, pp. 392–408. Springer, 2022.

## Appendix Overview

This appendix provides additional material to support the main paper, organized as follows:

1. Section **A** presents additional model details.
2. Section **B** describes implementation and training details.
3. Section **C** reports extended ablation studies and additional quantitative results.
4. Section **D** details the construction, annotation protocol, and evaluation splits of the CAAD-3K dataset.
5. Section **E** provides full quantitative results across all benchmarks.
6. Section **F** discusses limitations and directions for future work.
7. Section **G** presents additional qualitative results.

## A. Additional Model Details

This appendix provides full specifications of the model components summarized in Section 5, including (i) Context-Selective Residuals (CSR), (ii) text refinement and losses, (iii) the Compatibility Reasoning Module (CRM), and (iv) inference for image- and pixel-level scoring.

### A.1. Detailed Proof of Proposition 4.1

*Proof.* Let the two observations be defined as  $x = g(a, c)$  and  $x' = g(a, c')$ . By assumption, the intrinsic representations of these observations are identical:

$$\phi(x) = \phi(g(a, c)) = \phi(g(a, c')) = \phi(x'). \quad (6)$$

The detector is defined as the composition  $f(x) = \psi(\phi(x))$ . Applying this to our observations:

$$f(x) = \psi(\phi(x)) = \psi(\phi(x')) = f(x'). \quad (7)$$

For  $f$  to be correct on an input, its prediction must match the ground truth label  $y$ . Thus, simultaneous correctness on both  $x$  and  $x'$  requires:

$$f(x) = h(a, c) \quad \text{and} \quad f(x') = h(a, c'). \quad (8)$$

However, the proposition assumes the labels are distinct:  $h(a, c) \neq h(a, c')$ . Combining these equalities leads to a contradiction:

$$h(a, c) = f(x) = f(x') = h(a, c'). \quad (9)$$

Since  $h(a, c) \neq h(a, c')$  is given, the condition  $f(x) = f(x')$  implies  $f$  cannot match the ground truth for both inputs.  $\square$

### A.2. Context-Selective Residuals (CSR)

Let  $f_\theta$  denote the pretrained CLIP (Radford et al., 2021) visual transformer. For an input image  $x$ , we construct three views: subject-focused  $x_s$ , context-focused  $x_c$ , and global  $x_g$ . Let  $m \in \{0, 1\}^{H \times W}$  denote a binary foreground mask, where  $m_{ij} = 1$  indicates subject pixels.

The subject-focused and context-focused views are constructed by pixel-wise masking in the image space:

$$x_s = m \odot x, \quad x_c = (1 - m) \odot x, \quad (10)$$

where  $\odot$  denotes element-wise multiplication. Pixels outside the masked region are set to zero, consistent with CLIP preprocessing. No bounding-box cropping or spatial resizing is performed. The global view is defined as  $x_g = x$ .

During training on CAAD-3K, instance-level foreground masks are provided with the dataset. When masks are unavailable, we use automatically generated segmentation masks (e.g., from generic segmentation models) as a drop-in replacement. Subject–context separation is used only to obtain region-specific embeddings during training and is not required at inference.

Passing each view through the shared backbone produces token sequences  $\{X_s^{(i)}\}_{i=0}^{L_v}$ ,  $\{X_c^{(i)}\}_{i=0}^{L_v}$ , and  $\{X_g^{(i)}\}_{i=0}^{L_v}$ , where  $X_b^{(i)} \in \mathbb{R}^{N \times D}$  denotes the token matrix at transformer layer  $i$  (including the class token),  $L_v$  is the number of visual layers,  $N$  is the number of tokens, branch  $b \in \{s, c, g\}$  and  $D$  is the embedding dimension.

CSR inserts a lightweight, branch-specific residual adapter in the first  $K$  transformer layers (we use  $K=6$ ). For layer  $i \in \{1, \dots, K\}$ :

$$X_b^{(i)} \leftarrow (1 - \lambda_i) X_b^{(i)} + \lambda_i \text{CSR}_b^{(i)}(X_b^{(i)}), \quad (11)$$

where  $\lambda_i \in [0, 1]$  is a learnable parameter, and  $\text{CSR}_b^{(i)}$  denotes a branch-specific residual module. Layers  $i > K$  remain unchanged, preserving the pretrained backbone.

From the final layer tokens  $X_b^{(L_v)}$ , we extract (i) a global embedding (class token) and (ii) patch embeddings:

$$\begin{aligned} \tilde{z}_b &= X_b^{(L_v)}[\text{cls}] \in \mathbb{R}^D, \\ \tilde{P}_b &= X_b^{(L_v)}[\text{patch}] \in \mathbb{R}^{(N-1) \times D}. \end{aligned} \quad (12)$$

We denote  $\tilde{z}_s, \tilde{z}_c, \tilde{z}_g$  as the refined subject, context, and global embeddings used throughout Section 5.

### A.3. Text Refinement and Contextual Text Embeddings

Let  $g_\psi$  denote the CLIP text transformer with  $L_t$  layers. Given a class/action description prompt, we produce two text embeddings representing the *normal* and *anomalous*

contextual interpretations:  $t_0$  and  $t_1$ . To enable context-conditioned semantics without full finetuning, we adapt only the first  $L$  text layers (we use  $L=3$ ) via a gated residual pathway:

$$Z^{(i)} \leftarrow (1 - \gamma_i) Z^{(i)} + \gamma_i \text{TR}^{(i)}(Z^{(i)}), \quad i = 1, \dots, L, \quad (13)$$

where  $Z^{(i)} \in \mathbb{R}^{M \times D}$  is the text token matrix at layer  $i$ ,  $\gamma_i \in [0, 1]$  is a learnable gate, and  $\text{TR}^{(i)}$  is a two-layer MLP. The final pooled text embedding is normalized to unit length. We denote the refined embeddings as  $\tilde{t}_0, \tilde{t}_1$ .

#### A.4. Text Disentanglement Objectives

Contextual anomaly detection requires the text embedding space to represent context-dependent semantic states of the same concept (i.e., whether an object or action is compatible with its scene). To this end, the refined text encoder produces paired normalized embeddings  $\tilde{t}_0$  (normal) and  $\tilde{t}_1$  (anomalous) for each class, which are optimized using complementary disentanglement objectives.

**Orthogonality loss.** To prevent collapse between normal and anomalous interpretations, we encourage  $\tilde{t}_0$  and  $\tilde{t}_1$  to occupy distinct directions in the embedding space. This is achieved via cosine decorrelation:

$$\mathcal{L}_{\text{ortho}} = \langle \tilde{t}_0, \tilde{t}_1 \rangle^2. \quad (14)$$

This constraint ensures that contextual violation is encoded as a meaningful semantic deviation rather than a small perturbation. The weight of this loss is annealed during early training to avoid instability.

**Intra-class consistency loss.** While separated, both variants should preserve the same class identity. We therefore constrain them to remain close to a shared prototype  $\tilde{t}_\mu = \frac{1}{2}(\tilde{t}_0 + \tilde{t}_1)$ :

$$\mathcal{L}_{\text{cons}} = \frac{1}{2} \left( \|\tilde{t}_0 - \tilde{t}_\mu\|_2^2 + \|\tilde{t}_1 - \tilde{t}_\mu\|_2^2 \right). \quad (15)$$

**Image-text grounding loss.** To keep the disentangled text space aligned with visual semantics, we additionally align the prototype  $\tilde{t}_\mu$  with the corresponding visual class token  $\mathbf{v}_{\text{cls}}$ :

$$\mathcal{L}_{\text{ground}} = 1 - \text{sim}(\mathbf{v}_{\text{cls}}, \tilde{t}_\mu). \quad (16)$$

The full text objective is

$$\mathcal{L}_{\text{text}} = \lambda_{\text{ortho}} \mathcal{L}_{\text{ortho}} + \lambda_{\text{cons}} \mathcal{L}_{\text{cons}} + \lambda_{\text{ground}} \mathcal{L}_{\text{ground}}, \quad (17)$$

balancing semantic separation, identity preservation, and visual grounding.

#### A.5. Compatibility Scores and CRM

Given refined visual embeddings  $\tilde{z}_s, \tilde{z}_c, \tilde{z}_g \in \mathbb{R}^D$  and refined text embeddings  $\tilde{t}_0, \tilde{t}_1 \in \mathbb{R}^D$ , we compute per-branch compatibility via cosine similarity:

$$S_b^{(k)} = \text{sim}(\tilde{z}_b, \tilde{t}_k), \quad b \in \{s, c, g\}, k \in \{0, 1\}. \quad (18)$$

CRM performs *text-conditioned* aggregation over branches using single-head attention to infer adaptive fusion weights. We use the anomaly text embedding  $\tilde{t}_1$  to form a query:

$$q = W_q \tilde{t}_1 \in \mathbb{R}^{D_a}, \quad (19)$$

and project branch embeddings into an attention space to form keys:

$$K = [W_k \tilde{z}_s \quad W_k \tilde{z}_c \quad W_k \tilde{z}_g] \in \mathbb{R}^{D_a \times 3}, \quad (20)$$

where  $W_q$  and  $W_k$  are learned linear projections and  $D_a$  denotes the attention dimension.

The branch weights are computed as:

$$\boldsymbol{\alpha} = \text{softmax} \left( \frac{q^\top K}{\sqrt{D_a}} \right) \in \mathbb{R}^3, \quad \boldsymbol{\alpha} = [\alpha_s, \alpha_c, \alpha_g]. \quad (21)$$

The attention weights  $\boldsymbol{\alpha}$  are then used to aggregate branch representations in the original embedding space:

$$\tilde{z}_{\text{crm}} = \sum_{b \in \{s, c, g\}} \alpha_b \tilde{z}_b \in \mathbb{R}^D. \quad (22)$$

CRM introduces two properties absent from prior CLIP-based anomaly detectors. First, fusion is explicitly *text-conditioned*, enabling the model to infer whether incompatibility arises from the subject, the surrounding context, or their joint composition, rather than relying on static feature aggregation. Second, this reasoning generalizes to unseen classes, since the attention weights  $\boldsymbol{\alpha}$  are derived from language embeddings rather than learned per category. To prevent single-branch dominance and ensure stable training, we regularize the attention entropy and encourage consistency between fused and per-branch compatibility scores.

#### A.6. Image-Space Supervision

Image-space supervision enforces contextual compatibility at both global and local levels across the three visual branches. For each branch  $b \in \{s, c, g\}$ , the CSR-adapted visual encoder produces a branch-specific detection token  $f_b \in \mathbb{R}^D$  and a set of patch embeddings.

Each branch contributes an image-level classification loss that encourages correct discrimination between contextually normal and anomalous states. Let  $y \in \{0, 1\}$  denote the

ground-truth contextual anomaly label, where  $y = 1$  indicates an anomalous subject–context pair. Given the refined text embeddings  $(\tilde{t}_0, \tilde{t}_1)$ , we define a cross-entropy loss over the cosine similarities:

$$\mathcal{L}_{\text{img}}^{(b)} = \text{CE}([\text{sim}(\tilde{z}_b, \tilde{t}_0), \text{sim}(\tilde{z}_b, \tilde{t}_1)], y), \quad (23)$$

where  $\text{CE}(\cdot, y)$  denotes the standard softmax cross-entropy loss applied to a two-class logit vector with target label  $y$ . This loss encourages branch-level representations to assign higher compatibility to the correct contextual state.

### A.7. Fusion-Level Supervision

In addition to branch-level supervision, we apply losses to the CRM-aggregated representation to enforce coherent cross-branch reasoning. Let  $\tilde{z}_s, \tilde{z}_c, \tilde{z}_g$  denote the refined visual embeddings and let

$$\tilde{z}_{\text{crm}} = \sum_{b \in \{s, c, g\}} \alpha_b \tilde{z}_b$$

be the CRM-aggregated embedding, where  $\alpha$  are attention weights inferred from text.

An image-level cross-entropy loss is applied to the CRM-aggregated representation using refined text embeddings  $(\tilde{t}_0, \tilde{t}_1)$ :

$$\mathcal{L}_{\text{fuse-img}} = \text{CE}([\text{sim}(\tilde{z}_{\text{crm}}, \tilde{t}_0), \text{sim}(\tilde{z}_{\text{crm}}, \tilde{t}_1)], y). \quad (24)$$

To stabilize fusion, we introduce two regularizers. A consistency loss aligns fused logits with the mean branch logits,

$$\mathcal{L}_{\text{fuse-cons}} = \left\| \ell_{\text{crm}} - \frac{1}{3} \sum_b \ell_b \right\|_2^2, \quad (25)$$

and an attention entropy penalty prevents collapse onto a single branch,

$$\mathcal{L}_{\text{fuse-ent}} = -H(\alpha). \quad (26)$$

### A.8. Overall Training Objective

The training objective consists of image-space and text-space losses:

$$\mathcal{L}_{\text{total}} = \mathcal{L}_{\text{img}} + \mathcal{L}_{\text{text}} \quad (27)$$

Image-space supervision aggregates branch-level and fusion-level losses:

$$\begin{aligned} \mathcal{L}_{\text{img}} = & \sum_{b \in \{\text{fg, bg, full}\}} \mathcal{L}_{\text{img}}^{(b)} + \mathcal{L}_{\text{fuse-img}} \\ & + \lambda_{\text{fuse-cons}} \mathcal{L}_{\text{fuse-cons}} + \lambda_{\text{fuse-ent}} \mathcal{L}_{\text{fuse-ent}} \end{aligned} \quad (28)$$

The choice of loss weights and their sensitivity are analyzed later in section Section B.4.

Text-space supervision combines disentanglement objectives:

$$\mathcal{L}_{\text{text}} = \lambda_{\text{ortho}} \mathcal{L}_{\text{ortho}} + \lambda_{\text{cons}} \mathcal{L}_{\text{cons}} + \lambda_{\text{ground}} \mathcal{L}_{\text{ground}} \quad (29)$$

### A.9. Anomaly Scoring and Inference

**Image-level Scoring and I-AUROC** At inference time, an input image is processed by the three CSR branches and aggregated by the CRM, producing a fused representation  $\tilde{z}_{\text{crm}} \in \mathbb{R}^D$ . Let  $(\tilde{t}_0, \tilde{t}_1)$  denote the refined text embeddings corresponding to the contextually normal and anomalous interpretations of the class.

The image-level anomaly score is computed as a cosine margin between anomalous and normal compatibility:

$$s(x) = \sigma(\text{sim}(\tilde{z}_{\text{crm}}, \tilde{t}_1) - \text{sim}(\tilde{z}_{\text{crm}}, \tilde{t}_0)), \quad (30)$$

where  $\text{sim}(\cdot, \cdot)$  denotes cosine similarity and  $\sigma$  is the sigmoid function mapping scores to  $[0, 1]$ . Higher scores indicate stronger subject–context incompatibility. Inference requires no gradient updates or prompt tuning and is performed in a single forward pass.

**Pixel-level Scoring and P-AUROC** For pixel localization, we compute patch-level anomaly scores from the refined patch tokens  $\tilde{P}_s, \tilde{P}_c, \tilde{P}_g$ . Let  $\tilde{p}_{b,j} \in \mathbb{R}^D$  be the  $j$ -th patch embedding of branch  $b$  (normalized). We compute patch margins:

$$m_{b,j} = \text{sim}(\tilde{p}_{b,j}, \tilde{t}_1) - \text{sim}(\tilde{p}_{b,j}, \tilde{t}_0). \quad (31)$$

We aggregate branch patch margins using the *same* CRM weights  $\alpha$  from Eq. (21):

$$m_j = \alpha_s m_{s,j} + \alpha_c m_{c,j} + \alpha_g m_{g,j}. \quad (32)$$

The patch scores  $\{m_j\}$  are reshaped to the spatial token grid and bilinearly upsampled to the image resolution, yielding a pixel map  $M(x) \in \mathbb{R}^{H \times W}$ . P-AUROC is computed by thresholding  $M(x)$  against pixel-level ground truth masks on datasets where such masks exist (MVTec-AD, VisA, and CAAD-3K where applicable).

### A.10. Few-Shot Training Protocol

**CAAD-3K Few-Shot Protocol** For CAAD-3K, we adopt a *balanced few-shot* protocol applied uniformly to all methods. In an  $N$ -shot setting, the model is trained using  $N$  contextually normal and  $N$  contextually anomalous images per subject/action class, sampled uniformly at random from the CAAD-SS training split. This balanced supervision is required for discriminative contextual anomaly detection and does not provide privileged information relative to any baseline. For completeness, we additionally report results under a *normal-only* training variant in Section C.1.

Text prompts are fixed per class and reused across shots; no prompt engineering or test-time adaptation is performed. All parameters are optimized only on the selected few-shot subset, and evaluation is conducted on CAAD-CC to assess cross-context generalization.

**Standard Benchmarks: Zero-Shot Transfer** For MVTec-AD and VisA, we follow the standard cross-dataset zero-shot protocol used by prior work (Ma et al., 2025). The model is trained on the full training split of one dataset and evaluated directly on the other, without using any image-level supervision from the target dataset. At inference time, class information is provided only through text prompts, with no test-time adaptation.

### A.11. Region Supervision and Mask Robustness

Subject–context separation is used only to obtain region-specific visual embeddings during training and is not required at inference. Importantly, our framework does not rely on precise ground-truth annotations: instance masks can be replaced by automatically generated masks (e.g., from generic segmentation models) without modifying the model or training objective.

We use region masks solely to partition visual features into subject- and context-focused representations; no pixel-level anomaly labels or dense supervision are used. All reported results at test time are obtained without access to ground-truth masks. This design ensures that CoRe-CLIP does not depend on privileged supervision and remains applicable in real-world settings where accurate annotations are unavailable. This design ensures fair and directly comparable evaluation with all baselines in Table 1.

## B. Implementation Details

### B.1. Training Protocols

CoRe-CLIP is trained in two sequential stages using joint optimization over all losses. We do not employ mixed precision, gradient clipping, or balanced batching; instead, the stability of training arises from the modular design of CSR Section 5.2, the refined text encoder Section 5.3, and CRM Section 5.4.

**Batch size.** Unless otherwise specified, text refinement is performed with a batch size of 16, while visual CSR and CRM training uses a batch size of 8 images.

**Stage 1: Text Refinement:** The first  $L=3$  layers of the CLIP text encoder are adapted for 5 epochs using the orthogonality, consistency, and grounding losses described in the Section A.4. All visual parameters remain frozen in this stage.

**Stage 2: Visual CSR and CRM Training:** The CSR modules and CRM fusion block are trained end-to-end for an additional 20 epochs, with the CLIP (Radford et al., 2021) backbone kept frozen throughout. Training uses Adam (Kingma & Ba, 2017) with a learning rate of  $5 \times 10^{-5}$  and

cosine decay. Each batch consists of raw image–text pairs; no per-epoch resampling or prompt-level augmentation is required.

**Branch Usage Across Datasets:** For datasets containing meaningful subject and context structure (e.g., CAAD-3K), all three branches (subject, context, global) are active during training and inference. For datasets lacking explicit context variation (e.g., MVTec-AD (Bergmann et al., 2019), VisA (Zou et al., 2022)), the CRM automatically reduces to using only the full-image branch without requiring any architectural change. This ensures consistent training behavior across varied dataset types while preserving the integrity of the full model.

### B.1.1. HARDWARE AND SOFTWARE SETUP

All CAAD-3K experiments are conducted on a single NVIDIA A100 80GB GPU using PyTorch 2.2.2 with CUDA 12.1. Training is efficient: text–encoder refinement requires roughly 10 minutes, and CSR adaptation an additional 20 minutes. No multi-GPU synchronization or distributed training was required.

### B.2. Optimization and Hyperparameters

All optimization is performed using Adam (Kingma & Ba, 2017) with  $(\beta_1, \beta_2) = (0.5, 0.999)$ . Table 7 summarizes the default hyperparameters used for CAAD-3K, which were kept fixed across all experiments unless otherwise noted.

Table 7. Core hyperparameters used in training (default configuration for CAAD-3K).

Component	Setting
Text learning rate	$2 \times 10^{-5}$
Image learning rate	$3 \times 10^{-4}$
Text refinement depth	$L = 3$ layers
Image adaptation depth	$K = 6$ layers
<b>Text-space loss weights (Eq. 29)</b>	
$\lambda_{\text{ortho}}$	0.10 (annealed)
$\lambda_{\text{cons}}$	0.10
$\lambda_{\text{ground}}$	0.05
$\lambda_{\text{calib}}$	0 (CAAD-3K; used only for MVTec/VisA)
<b>Fusion loss weights (Eq. 28)</b>	
$\lambda_{\text{fuse-img}}$	1.0
$\lambda_{\text{fuse-cons}}$	0.5
$\lambda_{\text{fuse-ent}}$	0.05
Scheduler	MultiStepLR (milestones: 16k, 32k; $\gamma = 0.5$ )

For CAAD-3K, the default configuration above consistently produced strong results and required no further tuning. For MVTec-AD (Bergmann et al., 2019), competitive performance was obtained using moderate learning rates: text LR in the  $2 \times 10^{-5}$  range and image LR in the  $10^{-4}$  range, combined with 20 epochs of CSR adaptation. For VisA (Zou et al., 2022), which exhibits higher intra-class appearance

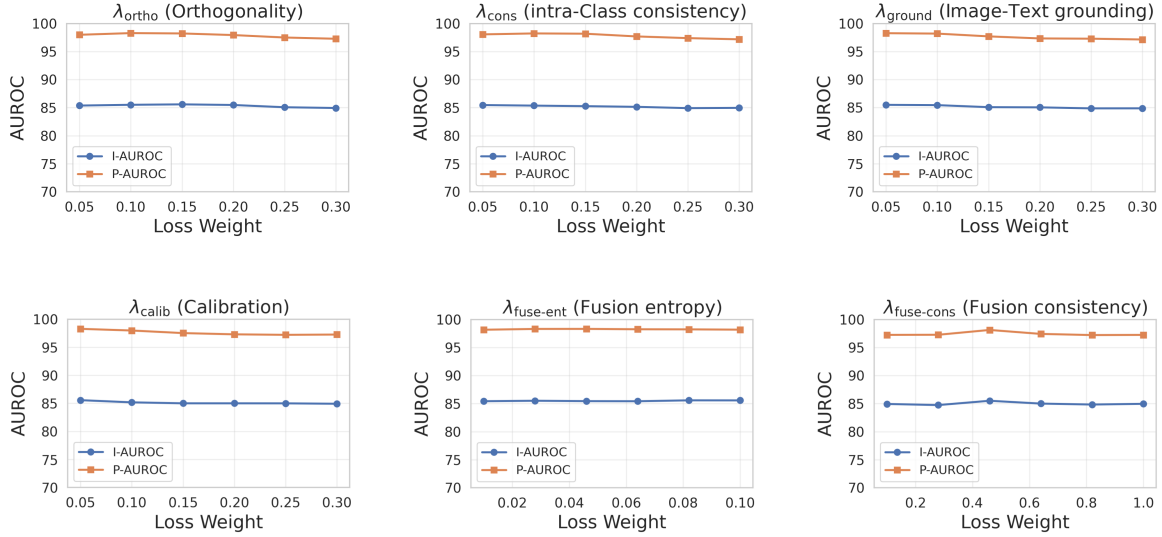


Figure 5. Loss-weight sensitivity analysis on CAAD-3K (4-shot). Each curve shows the effect of varying a single loss-term weight while keeping all others fixed at their default values. The model remains stable across a broad range of weights for both text-space objectives and CRM fusion regularizers, demonstrating that CoRe-CLIP is not overly sensitive to hyperparameter tuning.

diversity, we found that slightly elevated image learning rates and marginally stronger text-regularization weights provided the best performance. These adjustments remain small in magnitude and do not alter the training procedure, confirming that CoRe-CLIP is robust across datasets without dataset-specific engineering.

### B.3. Text Encoder Refinement Setup

The text encoder is adapted using the context selective residual pathway described in Section A.3. Since this modification affects only the first few transformer layers, the refinement remains parameter-efficient and preserves CLIP’s zero-shot alignment.

**Prompt Construction:** To generate paired normal and anomalous text embeddings, we use a small set of templated descriptions. For a class label  $cls$ , prompts are instantiated from the following sets:

- **Normal context:** “*a photo of  $cls$  in a normal place*”, “*a  $cls$  in a typical environment*”, “*a  $cls$  in a safe context*”, “*a usual photo of  $cls$* ”.
- **Anomalous context:** “*a  $cls$  in an unusual place*”, “*a  $cls$  in an abnormal environment*”, “*a  $cls$  in an unsafe context*”, “*an unusual photo of  $cls$* ”.
- **Formatting templates:** “ $cls$ .”, “*a photo of  $cls$ .*”, “*an image of  $cls$ .*”

The final embeddings  $(\tilde{t}_0, \tilde{t}_1)$  are obtained by averaging multiple prompt instantiations, which stabilizes semantic separation and reduces prompt sensitivity.

**Contrastive Calibration:** For certain datasets with low contextual variability, we observe that an additional margin-based calibration loss can further enhance text–image alignment:

$$\mathcal{L}_{\text{calib}} = [m - \langle v_{\text{cls}}, t_1 \rangle + \langle v_{\text{cls}}, t_0 \rangle]_+. \quad (33)$$

This term encourages anomalous images to align more strongly with anomalous text than with normal text, but is highly dataset dependent (e.g., effective on MVTec-AD (Bergmann et al., 2019)) and therefore excluded from the main configuration.

### B.4. Loss Weight Selection

CoRe-CLIP is trained using a combination of text-level, image-level, and fusion-level objectives. For clarity, we restate the losses here and describe how their weights are selected; complete formulations appear in the main paper.

**Text–space loss weighting:** The refined text embeddings  $(\tilde{t}_0, \tilde{t}_1)$  are trained using four components: orthogonality  $\mathcal{L}_{\text{ortho}}$ , intra-class consistency  $\mathcal{L}_{\text{cons}}$ , image–text grounding  $\mathcal{L}_{\text{ground}}$ , and an optional margin-based contrastive calibration  $\mathcal{L}_{\text{calib}}$  term (used only for MVTec-AD (Bergmann et al., 2019)).

During training, the orthogonality and classification-related weights are annealed over the first 30–50% of text-adaptation epochs to prevent early collapse. Empirically, we use  $\lambda_{\text{ortho}} \in [0.1, 0.15]$ ,  $\lambda_{\text{cons}} = 0.1$ ,  $\lambda_{\text{ground}} = 0.05$ , and a small calibration weight  $\lambda_{\text{calib}} \in [0.02, 0.05]$  when enabled. These choices were validated through a sweep over the range  $[0.05, 0.3]$  for each term, with CAAD-3K,

**Table 8. Normal-only training ablation on CAAD-3K (Cross-Context).** Few-shot performance when only normal images are available during training. Results are reported as Image-AUROC (I) and Pixel-AUROC (P). CoRe-CLIP maintains a large margin over all baselines, indicating robustness to the absence of anomalous supervision. **Best** and **second-best** results are highlighted.

Method	Venue	1-shot		2-shot		4-shot	
		I-AUROC	P-AUROC	I-AUROC	P-AUROC	I-AUROC	P-AUROC
CLIP (Radford et al., 2021)	ICML 2021	35.0	40.5	34.4	42.3	39.5	54.5
CRTNet (Bomatter et al., 2021)	ICCV 2021	52.0	55.5	55.2	57.0	58.5	65.8
WinCLIP (Jeong et al., 2023)	CVPR 2023	55.4	57.5	57.3	60.7	59.2	65.7
AnomalyCLIP (Zhou et al., 2023)	ICLR 2024	54.4	62.9	56.5	67.0	58.5	71.8
AdaCLIP (Cao et al., 2024)	ECCV 2024	49.8	42.3	47.2	45.4	45.0	49.4
PromptAD (Li et al., 2024)	CVPR 2024	47.5	51.0	58.2	50.2	52.5	57.3
AA-CLIP (Ma et al., 2025)	CVPR 2025	42.0	60.1	43.7	63.5	45.1	60.4
IIPAD (Lv et al., 2025)	ICLR 2025	41.0	50.2	40.5	55.6	42.2	54.9
CoRe-CLIP (ours)		<b>71.2</b>	<b>73.2</b>	<b>70.4</b>	<b>72.5</b>	<b>74.3</b>	<b>80.3</b>

MVTec-AD, and VisA showing consistent optima around the values reported above.

**Image-space losses:** Each visual branch (subject, context, global) is supervised using an image-level compatibility loss between normal and anomalous text embeddings, as defined in Eq. (23). The same loss weight is applied to all branches. Empirical sensitivity analysis shows stable performance for coefficients in the range [0.05, 0.15] on CAAD-3K.

**Fusion losses:** We apply fusion-level supervision and regularization as defined in Appendix A.7. Unless otherwise noted, we use  $\lambda_{\text{fuse-img}} = 1.0$ ,  $\lambda_{\text{fuse-cons}} = 0.5$ , and  $\lambda_{\text{fuse-ent}} = 0.05$ , validated via sensitivity sweeps Figure 5.

#### Hyperparameter robustness:

Figure 5 summarizes the effect of independently sweeping each loss coefficient. Across all six components, Image AUROC remains stable, with variations confined to a narrow band around the 4-shot baseline. Each loss exhibits a clear and stable optimum near its intended operating region (e.g.,  $\lambda_{\text{ortho}} \in [0.10, 0.15]$ ,  $\lambda_{\text{cons}} = 0.10$ ,  $\lambda_{\text{ground}} = 0.05$ ,  $\lambda_{\text{calib}} \in [0.02, 0.05]$ ,  $\lambda_{\text{fuse-cons}} = 0.5$ ,  $\lambda_{\text{fuse-ent}} = 0.05$ ). Overall, no loss term introduces sensitivity or training instability: even large deviations from the optimal range lead to only marginal performance changes. This indicates that CoRe-CLIP’s multi-component objective is well-conditioned and robust to hyperparameter choice.

## C. Extended Ablation Studies

### C.1. Effect of Normal-Only Training

Some anomaly detection methods are designed under the assumption that only normal samples are available during

training. To assess robustness under this stricter setting and ensure fair comparison, we evaluate all methods on CAAD-3K using a normal-only few-shot protocol, where only  $N$  normal images per class are provided and no anomalous images are used during training.

Table 8 reports the results under this protocol. As expected, performance decreases for all methods, reflecting the increased difficulty of contextual anomaly detection without exposure to incompatible subject–context examples. Importantly, CoRe-CLIP continues to outperform all baselines by a large margin across all shot regimes.

These results indicate that the improvements achieved by CoRe-CLIP are not driven by access to anomalous supervision, but instead stem from its explicit modeling of subject–context compatibility. The relative performance ordering is preserved under both balanced and normal-only training, demonstrating the robustness of conditional compatibility learning.

### C.2. Ablation of Text-Space Disentanglement Losses

A core contribution of CoRe-CLIP is the structured refinement of the CLIP text embedding into a context-sensitive normal/anomalous pair. The refinement module uses four complementary losses: (i) orthogonality, (ii) intra-class consistency, (iii) image–text grounding, and (iv) contrastive calibration. To isolate their contributions, we perform an ablation on the 4-shot CAAD-CC setting, removing one loss at a time while keeping all other training components unchanged (Table 9).

**Findings:** (1) *Orthogonality* provides the strongest individual gain, preventing normal and anomaly embeddings from drifting toward the same direction under low-data set-

tings. (2) *Consistency* stabilizes the refinement dynamics, improving both image- and pixel-level AUROC by reducing variance across shots. (3) *Grounding* is essential for maintaining semantic alignment with the visual space; removing it disproportionately harms pixel-level localization. (4) *Calibration* provides a smaller but reliable improvement, sharpening the separation between normal and anomalous contexts. The full model clearly outperforms all reduced variants, demonstrating that all four losses contribute complementary benefits.

**Table 9. Ablation of text-space disentanglement losses on CAAD-CC (4-shot).** Removing any component degrades performance, with grounding and orthogonality having the largest impact. The complete loss formulation yields the best separation of contextual normality vs. anomaly in both image- and pixel-level metrics.

Configuration	I-AUROC	P-AUROC
<b>Full CoRe-CLIP (all losses)</b>	<b>87.3</b>	<b>98.3</b>
w/o Orthogonality	82.7	96.9
w/o Consistency	83.4	97.4
w/o Grounding	82.1	95.8
w/o Calibration	84.5	98.0
Only CE (no text losses)	80.3	94.2

### C.3. Ablation of CSR Branches and CRM Fusion

To quantify the contribution of CSR Section A.2 and the CRM Section A.5 fusion mechanism, we conduct a systematic ablation on CAAD-CC (4-shot), evaluating all meaningful combinations of the subject (**s**), context (**c**), and global (**g**) branches. While single-branch performance has already been analyzed in the main paper Table 5, we extend this study by evaluating multi-branch combinations and the role of text-conditioned fusion.

**Table 10. Ablation of CSR branch combinations and CRM fusion on CAAD-CC (4-shot).** CRM is applied only when multiple branches are present. Only the full tri-branch configuration with CRM attains strong, context-sensitive anomaly reasoning.

g	s	c	CRM	I-AUROC	P-AUROC
✓	✓	✗	✗	78.4	91.2
✓	✗	✓	✗	74.1	86.7
✗	✓	✓	✗	79.5	88.9
✓	✓	✗	✓	82.7	95.1
✓	✗	✓	✓	80.3	92.8
✗	✓	✓	✓	81.5	93.6
✓	✓	✓	✗	81.2	93.1
✓	✓	✓	✓	<b>87.3</b>	<b>98.3</b>

**Findings:** (1) Two-branch models without CRM improve

over single-branch baselines, but remain limited because no single pairing captures the full subject-scene relation. (2) CRM consistently boosts all multi-branch configurations, confirming that simple concatenation or averaging cannot replace adaptive, text-conditioned branch selection. (3) Global+subject+context without CRM performs worse than some two-branch+CRM variants, showing that multi-branch inputs alone are insufficient; the fusion mechanism is indispensable. (4) The tri-branch + CRM model achieves the highest I-AUROC and P-AUROC, demonstrating that contextual anomalies require coordinated evidence from subject, context, and global-scene reasoning.

**Fusion Mechanism Comparison:** To ensure that CRM’s improvements are not attributable to generic feature mixing, we benchmark several alternative fusion strategies frequently used in multi-branch architectures: (i) simple averaging, (ii) learned static scalar weighting, and (iii) concatenation followed by a linear projection. All methods use the same three CSR branches (global+subject+context) and identical training settings. Results are shown in Table 11.

**Table 11. Comparison of fusion mechanisms** using the full tri-branch CSR representation on CAAD-CC (4-shot). Only CRM provides text-conditioned, context-sensitive aggregation.

Fusion Method	I-AUROC	P-AUROC
Average fusion	80.3	95.9
Static learned weights	81.0	96.4
Concat + Linear projection	81.5	96.8
<b>CRM (ours)</b>	<b>87.3</b>	<b>98.3</b>

**Fusion Findings:** These results highlight that: (1) *Naive averaging* underperforms because it forces all branches to contribute equally, regardless of anomaly context. (2) *Static learned weights* helps but still lacks anomaly- or prompt-specific selectivity. (3) *Concatenation+Projection* provides moderate gains, but cannot emulate the targeted, text-aware routing needed for contextual anomalies. (4) Only *text-conditioned CRM* adapts its branch weighting based on the anomaly description, enabling fine-grained subject-scene mismatch reasoning.

Overall, these ablations validate the architectural necessity of both the CSR multi-branch decomposition and the CRM attention fusion module, and highlight that the performance gains in CoRe-CLIP arise from principled reasoning design rather than from additive engineering.

### C.4. Adapter Parameter Efficiency and Model Size

While CoRe-CLIP introduces a multi-branch architectural design, it remains highly parameter-efficient relative to prior adaptation-based approaches as shown in Table 12. For

a fair comparison, we restrict evaluation to architectural-adaptation methods (e.g., adapters, fusion modules), excluding prompt-only baselines whose trainable parameter counts are orders of magnitude smaller by design and therefore not comparable in representational capacity.

**Table 12. Trainable-parameter comparison among architectural adaptation methods.** CoRe-CLIP achieves state-of-the-art performance on CAAD-3K, MVTec-AD (Bergmann et al., 2019), and VisA (Zou et al., 2022) while remaining competitively lightweight. When CoRe-CLIP automatically disables unused branches on texture-centric datasets (e.g., MVTec-AD (Bergmann et al., 2019), VisA (Zou et al., 2022)), the effective trainable fraction drops to 2.5%.

Method	Total Params	Trainable Params	% Trainable
AdaCLIP (Cao et al., 2024)	427.9M	5.56M	1.30%
AA-CLIP (Ma et al., 2025)	441.3M	12.58M	2.85%
HIPAD (Lv et al., 2025)	1987.8M	1560.2M	78.5%
<b>CoRe-CLIP (ours)</b>	463.6M	34.80M	7.5%
<b>CoRe-CLIP-A (ours)</b>	463.6M	11.5M	2.5%

**Discussion:** Although CoRe-CLIP trains a higher fraction of parameters than AdaCLIP (Cao et al., 2024) or AA-CLIP (Ma et al., 2025), this overhead is structurally constrained to the tri-branch contextual encoder and CRM fusion, rather than generic capacity expansion. To control for optimization capacity, we additionally report CoRe-CLIP-A, a capacity-matched variant that automatically disables unused branches and uses only 2.5% trainable parameters, comparable to existing adapter-based methods. Despite this reduction, CoRe-CLIP-A retains strong performance across benchmarks, indicating that the observed gains arise from the proposed multi-branch relational reasoning and conditional compatibility formulation rather than raw parameter count.

While Table 12 focuses on trainable parameter efficiency, inference-time cost is dominated by backbone forward passes. CoRe-CLIP incurs modest additional computation from parallel branch execution but does not rely on external models or segmentation at test time. On texture-centric datasets such as MVTec-AD (Bergmann et al., 2019) and VisA (Zou et al., 2022), the CRM collapses to a single-branch configuration, allowing CoRe-CLIP to remain nearly as lightweight as prior approaches while delivering substantially stronger accuracy.

### C.5. Few-shot Branch Selection Stability

To understand how CoRe-CLIP allocates reasoning capacity under varying supervision, we analyze the CRM attention weights for the subject, context, and global branches across 1-, 2-, and 4-shot settings (Fig. 6). The results show a remarkably stable pattern: (1) Subject and context remain the dominant contributors, consistently receiving 0.38–0.50 attention, confirming that contextual reasoning relies jointly on subject and environment cues. (2) Full-image attention

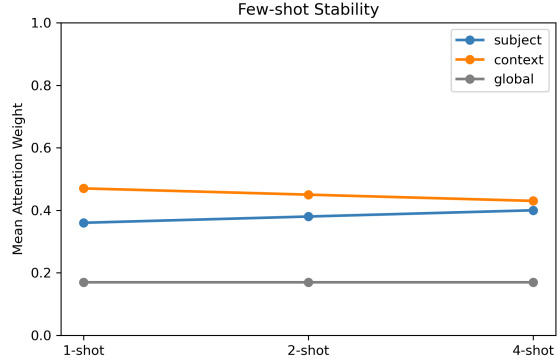


**Figure 6. Few-shot stability of CRM attention across branches on CAAD-CC.** Context and subject branches dominate consistently from 1-shot to 4-shot, confirming robust and interpretable branch selection.

stays low and nearly constant, indicating that the model avoids collapsing into global appearance cues even in extremely low-shot conditions. (3) As shots increase, subject attention rises slightly while context decreases mildly, suggesting that additional supervision helps the model refine object-centric signals without discarding context.

These trends verify that CoRe-CLIP’s tri-branch design behaves predictably and does not overfit to any single branch, preserving robust object–scene reasoning even in minimal-data regimes.

## D. CAAD-3K Dataset Details

CAAD-3K is a high-fidelity synthetic benchmark designed to study contextual anomaly detection, featuring complex scenes with multiple co-occurring objects where abnormality arises from object–scene incompatibility rather than appearance defects. The dataset consists of two complementary splits:

- CAAD-SS, the main benchmark containing 2,095 images covering a wide range of object categories and scene types, and
- CAAD-CC, a cross-context extension with 905 additional images rendered in unseen context distributions.

While CAAD-SS is used for training and validation, CAAD-CC serves as a held-out domain-shift test set, enabling systematic measurement of generalization to novel environments. Together, these splits provide a controlled yet diverse experimental setting for assessing context reasoning, ensuring that models cannot rely on memorized context or spurious correlations.

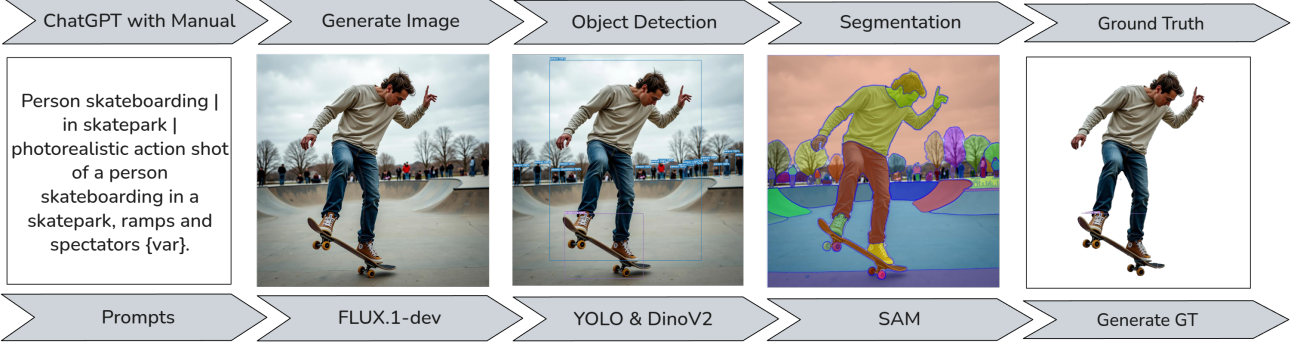


**Figure 7. CAAD-3K dataset generation pipeline.** An overview of the automated and human-curated process used to construct CAAD-3K. The pipeline integrates (i) GPT-4 (OpenAI, 2023) prompt synthesis, (ii) high-fidelity scene rendering with FLUX.1-dev (Labs, 2025), (iii) object localization using YOLOv8 (Jocher et al., 2023) and GroundingDINO (Liu et al., 2024), (iv) instance-level segmentation with SAM (Kirillov et al., 2023), and (v) manual quality verification. This design ensures fine-grained subject/context control and high contextual realism.

#### Algorithm 1 CAAD-3K Dataset Generation Pipeline

```

1: Input: Object classes  $\mathcal{C}$ ; normal/anomalous prompt
   templates
2: Output: Dataset  $\mathcal{D}$  with masks
3: for each class  $c \in \mathcal{C}$  do
4:   Generate normal/anomalous prompts using GPT-4
5:   Render  $N$  images per prompt using FLUX.1-dev
6:   Detect bounding boxes using YOLOv8 and Ground-
   ingDINO
7:   Extract masks using SAM
8:   if bbox missing or mask low-quality or scene unreal-
   istic then
9:     Discard sample
10:   else
11:     Append sample to  $\mathcal{D}$ 
12:   end if
13: end for

```

#### D.1. Pixel-Level Annotations

Contextual anomaly detection is inherently an image-level task, as abnormality arises from subject–context incompatibility rather than localized appearance defects. To remain compatible with standard anomaly detection benchmarks that report pixel-level metrics, CAAD-3K includes pixel annotations as a design convention. Specifically, when an image is labeled anomalous due to subject–context mismatch, the subject region is marked as anomalous. This choice enables P-AUROC evaluation but does not imply that contextual anomalies are intrinsically pixel-local. Accordingly, Image-AUROC is treated as the primary metric throughout the paper.

#### D.2. Dataset Creation Pipeline

The CAAD-3K dataset is generated through a multi-

stage pipeline designed to produce high-quality contextual anomaly samples while maintaining strict control over object–scene semantics. The pipeline integrates large language models for prompt engineering, state-of-the-art diffusion models for image synthesis, and foundation models for object detection and mask extraction, followed by human verification to ensure dataset reliability. An overview of the pipeline is provided in Fig. 7.

**Prompt Generation:** To ensure broad linguistic and contextual diversity, we use GPT-4 (OpenAI, 2023) to generate natural-language prompts describing both normal and anomalous object–scene combinations. For each of the 15 object categories, GPT-4 (OpenAI, 2023) is asked to propose: (i) contextually appropriate scenes, (ii) contextually incompatible or unsafe scenes, and (iii) variations in appearance, activity, lighting conditions, and spatial layout. Prompts are manually filtered to remove ambiguous instructions or ones likely to induce visual artifacts. This step guarantees semantic grounding and avoids biases caused by hand-written or template-based prompts. *Example prompt.* Boat | at marina | "photorealistic image of a pleasure boat tied at a marina pier{var}." Here, {var} is automatically expanded into diverse contextual modifiers.

**Image Synthesis:** We use the FLUX.1-dev diffusion model (Labs, 2025) to synthesize high-resolution images across diverse indoor, outdoor, urban, and natural environments. For each normal–anomalous prompt pair, we generate multiple samples with controlled sampling parameters to maintain stylistic and compositional consistency across the dataset. While the exact object instance may vary across generations, the object *category* and intended scene context remain fixed, ensuring that anomalies stem from object–scene incompatibility rather than appearance

artifacts. Images with geometric distortions, missing body parts, or implausible physics are removed.

**Object Localization:** We localize the primary object in each synthesized image using both YOLOv8 (Jocher et al., 2023) and GroundingDINO (Liu et al., 2024). YOLOv8 (Jocher et al., 2023) provides reliable bounding boxes for common object categories, but cannot handle fine-grained action prompts (e.g., “person running”) or uncommon generated categories (e.g., “fire”) absent from its label space. GroundingDINO (Liu et al., 2024), in contrast, performs open-vocabulary grounding using the textual prompt and can correctly identify action-conditioned or rare objects, but occasionally produces coarse or over-complete regions.

We therefore adopt a complementary strategy: YOLOv8 (Jocher et al., 2023) detections are used when the object class exists in its taxonomy, while GroundingDINO (Liu et al., 2024) detections are used for action-specific or open-vocabulary prompts. When both detectors return valid boxes, we select the spatially tighter region. This hybrid approach ensures robust localization across diverse object types and generative variations, even when the diffusion model introduces multiple objects or visually similar distractors.

**Mask Extraction:** Segmentations are obtained using the Segment Anything Model (SAM) (Kirillov et al., 2023), guided by the validated bounding boxes. Masks are inspected for connectivity, boundary quality, and alignment with the detected object. These instance masks provide the basis for subject extraction, context separation, and pixel-level anomaly evaluation. By construction, CAAD-3K provides reliable instance masks for every sample, a level of annotation that is typically unavailable or incomplete in real-world contextual datasets.

**Human Verification and Quality Control:** All images and masks undergo a final manual review. Annotators remove samples exhibiting unrealistic object placement, incorrect perspective, inconsistent shadows, or segmentation failures. Approximately 20% of generated samples are discarded through this process. The resulting dataset maintains high visual realism, semantically correct normal cases, and reliably anomalous contextual violations.

**On Synthetic Data Validity:** CAAD-3K leverages controllable text-to-image generation to model contextual anomalies that would be unsafe or impractical to capture in the real world. While synthetic, every sample is constructed to be visually plausible, semantically coherent, and statistically balanced across contexts, ensuring that the benchmark measures reasoning ability rather than low-level visual cues.

### D.3. Scene Object Pairing Strategy

A central requirement for contextual anomaly detection is a principled strategy for pairing objects with scenes such that the distinction between “normal” and “anomalous” arises from semantic compatibility, not from synthetic artifacts or spurious visual cues. To this end, CAAD-3K adopts a controlled but diverse scene-object pairing procedure.

**Normal Pairings:** For each of the 15 object categories, we compile a curated set of scene types where the object naturally occurs (e.g., motorbike–road, sofa–living room). These mappings are derived from web-scale co-occurrence statistics and validated manually to ensure contextual realism. Prompts sampled from this list form the normal subset.

**Anomalous Pairings:** Anomalous examples are created by pairing the same objects with semantically incompatible environments (e.g., motorbike–indoor, car–beach, person running–highway). Importantly, the object itself remains visually valid, only the contextual relation is violated. This prevents anomaly cues from collapsing into object corruption or generative artifacts.

**Distribution Control:** To avoid trivial cues (e.g., a specific context always indicating anomaly), each object class is associated with multiple normal and multiple anomalous scene types, covering indoor, outdoor, urban, and natural environments. No context appears exclusively in the normal or anomalous category, ensuring that models must rely on object–scene reasoning, not scene memorization.

**Prompt Diversity:** Within each pairing, GPT-4 (OpenAI, 2023) produces diverse paraphrases describing object appearance, actions, and camera viewpoints. This prevents linguistic overfitting and yields a broad range of visual instantiations rather than template-like repetitions.

**Reviewer Assurance:** Together, this strategy guarantees that contextual abnormality emerges from semantic relational mismatch, not from low-level artifacts, synthetic shortcuts, or bias in context frequency. The resulting dataset provides a rigorous testbed where success requires true context-aware reasoning.

### D.4. Class Composition

A central design goal of CAAD-3K is to construct a dataset where contextual anomalies are *semantically meaningful*, *visually plausible*, and *reflective of real-world subject–scene relationships*. To achieve this, we curate fifteen object and action categories that span vehicles, animals, human activities, furniture, and utilitarian objects. These categories are selected not for visual diversity alone, but because each embodies strong, learnable affordances with its surrounding

context. The resulting composition enables the study of *functional*, *behavioral*, and *ecological* anomalies, phenomena that cannot be captured by traditional appearance-based Anomaly Detection datasets.

#### D.4.1. COVERAGE OF RELATIONAL SEMANTICS

Contextual anomalies arise only when objects maintain stable, interpretable relationships with their environment. Accordingly, our class taxonomy reflects categories whose placement is governed by clear scene affordances:

- **Vehicles** (Aeroplane, Boat, Car\_parked, Motorbike): restricted to infrastructure such as roads, runways, waterfronts, or parking environments. Misplacements (e.g., vehicles indoors) produce strong violation signals.
- **Furniture and Utility Objects** (Sofa, Shopping\_cart, Camping\_tent): tied to indoor/outdoor or commercial/domestic contexts, allowing models to reason about functional scene compatibility.
- **Animals**: ecologically grounded and highly versatile, but anomalous in many structured indoor and industrial environments.
- **Human Actions** (Person\_running, Person\_cycling, Person\_riding\_horse, Person\_skateboarding, Person\_with\_umbrella, Child\_playing): the only class group that introduces *action–scene coherence*, enabling evaluation of contextual reasoning beyond static object placement.

This collection spans static objects, dynamic agents, and composite action–object states, ensuring that CAAD-3K supports a broad spectrum of contextual constraints and affords richer anomaly reasoning than previous datasets.

#### D.4.2. REAL-WORLD ANOMALY RELEVANCE

Each class corresponds to scenarios that are meaningful in real-world surveillance, robotics, and public-safety applications. Safety-critical situations (e.g., Fire, Child\_playing), transportation misuse (e.g., vehicles in constrained indoor spaces), and hazardous behaviors (e.g., running, cycling, or skateboarding in restricted areas) reflect categories where contextual violations carry practical consequences. Unlike earlier datasets that rely on synthetic novelty or texture-based deviations, CAAD-3K captures *functionally grounded anomalies* that models should robustly detect.

#### D.4.3. BALANCED DISTRIBUTION ACROSS NORMAL AND ANOMALOUS CONTEXTS

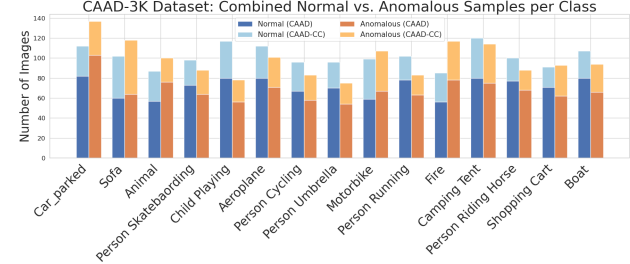


Figure 8. Per-class distribution of normal and anomalous samples across CAAD-SS and CAAD-CC. Each bar shows CAAD-SS and CAAD-CC counts as stacked segments, illustrating balanced object coverage and controlled contextual variability across all 15 classes.

To avoid bias toward specific contexts or classes, each category includes a balanced mixture of normal and anomalous samples. Figure 8 shows that CAAD-SS and the cross-context split CAAD-CC maintain nearly identical proportions of normal and anomalous examples within each category. This design prevents the model from exploiting class-specific frequency patterns and ensures that anomaly detection arises from learning contextual semantics rather than dataset imbalance.

#### D.4.4. CONTEXT DIVERSITY WITHIN CAAD-SS

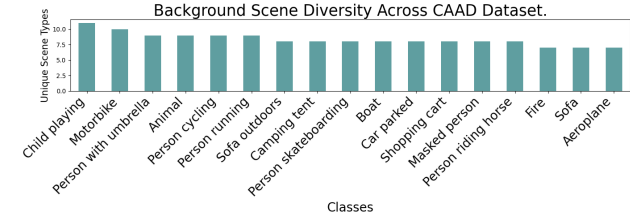


Figure 9. Context diversity across CAAD-SS dataset. CAAD-SS provides high contextual entropy, essential for evaluating object–scene compatibility.

Beyond class balancing, CAAD-SS is designed to expose each class to a diverse range of valid contexts, increasing contextual entropy and preventing overfitting to narrow scene distributions. Figure 9 summarizes the number of unique scene types per class in CAAD-SS. Most categories appear in 8–12 distinct environments. This diversity is crucial for evaluating whether models learn object–scene compatibility rather than simply memorizing context priors.

#### D.4.5. CONTEXTUAL DIVERSITY ACROSS SPLITS

A key goal of our dataset design is to ensure that CAAD-SS and CAAD-CC provide *complementary* yet *non-redundant*

contextual distributions. This is critical for evaluating robustness to context shift. We assess this through two quantitative analyses.

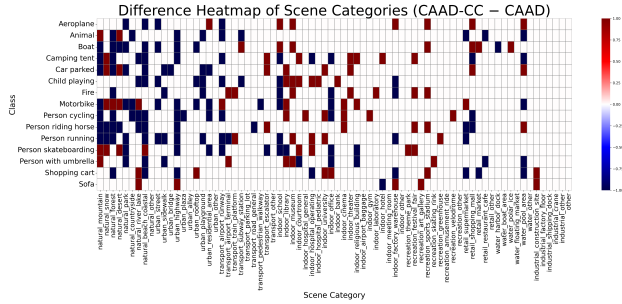


Figure 10. Difference heatmap of scene-category presence between CAAD-CC and CAAD-SS. Red cells indicate scene categories that appear in CAAD-CC but not in CAAD-SS for a given class, while blue cells indicate the opposite. The widespread and structured red-blue patterns demonstrate that CAAD-CC introduces substantial novel contextual diversity, confirming that the two dataset splits provide complementary context distributions.

**Difference Heatmap:** Figure 10 visualizes a binary difference matrix of scene-category presence across classes. Red cells indicate scene categories unique to CAAD-CC, and blue cells those unique to CAAD-SS. The widespread, structured pattern of red and blue confirms that CAAD-CC introduces a large set of novel, semantically meaningful contexts (e.g., institutional, industrial, recreational environments). Meanwhile, CAAD-SS retains its own set of distinct contexts, ensuring that the two splits remain contextually complementary rather than overlapping. This prevents split leakage and encourages generalization to unseen scene distributions.

**Jaccard Similarity:** To quantify the degree of contextual overlap per class, Figure 11 reports the Jaccard similarity between the set of scene categories associated with each class in the two splits. Similarities lie consistently in the 0.07–0.27 range, confirming low contextual redundancy. Importantly, the core class semantics remain shared, but the contexts are deliberately distinct. This property is central to challenging context-aware anomaly detection models in out-of-context generalization.

#### D.4.6. INTERPRETATION AND IMPLICATIONS

Considered together, these analyses demonstrate that CAAD-3K offers:

1. rich and balanced class-level semantics,
2. broad intra-class scene diversity, and
3. controlled inter-split contextual complementarity.

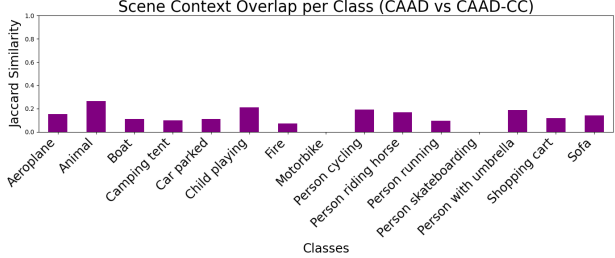


Figure 11. Per-class Jaccard similarity between the sets of scene categories in CAAD-SS and CAAD-CC. Similarity scores remain consistently low (0.07–0.27), indicating minimal overlap in contexts while preserving the semantic identity of each class. This low contextual redundancy is desirable for reliably evaluating models on context-sensitive anomaly detection.

The dataset is therefore not merely a large collection of images, but a *structured benchmark* for evaluating next-generation models that must reason about functional, environmental, and behavioral object–scene coherence. By maximizing contextual richness rather than raw quantity, CAAD-3K establishes a rigorous foundation for research on context-aware anomaly detection under realistic and systematically varied scene conditions.

#### D.5. Ethical and Safety Considerations

CAAD-3K is fully synthetic and contains no identifiable human subjects or copyrighted imagery. All text prompts are manually curated to avoid sensitive or harmful content. The dataset is intended exclusively for research on visual reasoning and anomaly detection, and not for surveillance, biometric analysis, or other high-stakes applications. We note that CoRe-CLIP relies on a pretrained CLIP backbone, which may encode social, cultural, or geographic biases from its web-scale training data; as a result, contextual compatibility judgments may reflect such normative assumptions, constituting a known limitation of foundation-model-based approaches.

### E. Full Quantitative Results

We report comprehensive per-class results for CoRe-CLIP across all benchmarks and training regimes in Tables 13 to 15. For **CAAD-CC**, supervision follows the few-shot protocol (1-, 2-, and 4-shot), while for **MVTec-AD** (Bergmann et al., 2019) and **VisA** (Zou et al., 2022), evaluation is strictly **zero-shot**, using supervision learned exclusively from the other dataset. All results are averaged over three independent runs with different random seeds; aggregate Image-AUROC exhibits low variance across runs, typically within  $\pm 0.6$  for CAAD-3K and  $\pm 0.4$  for MVTec-AD and VisA, indicating stable optimization. Per-class results are included for completeness but may exhibit higher variance in extreme few-shot regimes (1–2 shots), where performance is sensi-

tive to support-set sampling rather than model instability. Following prior work (Bergmann et al., 2019; Zou et al., 2022), we additionally report AUPR (area under the precision–recall curve) and PRO (per-region overlap) for completeness, using their standard definitions.

## F. Limitations and Future Work

While CoRe-CLIP establishes a principled framework for *reasoning-driven* contextual anomaly detection, several natural extensions remain open for future work.

**Dataset scope:** Although CAAD-3K avoids the ethical and practical challenges of acquiring real contextual violations, its coverage can still be expanded. Increasing the variety of subject–scene interactions, introducing richer behavioral cues, and incorporating more complex multi-object compositions would further broaden the space of contextual relations available for training and evaluation.

**Mixed-state contextual anomalies:** Our current formulation models contextual mismatch with respect to a dominant subject entity. Extending this to *partial* or *mixed-state* anomalies, where only certain parts or attributes of an object violate the scene context—would enable finer-grained reasoning and provide an additional challenge for future benchmarks.

**Context reasoning depth:** CRM employs a single-step, text-conditioned fusion to combine multi-branch evidence. Exploring richer mechanisms such as multi-hop inference, iterative refinement, or graph-based propagation could strengthen subject–scene coherence modeling while preserving the model’s interpretability.

Overall, these points represent *opportunities for advanc-*

*ing the context-aware paradigm*, rather than structural limitations of the approach. CoRe-CLIP provides a strong foundation on which broader contextual benchmarks and next-generation reasoning-centric anomaly detectors can be developed.

## G. Additional Qualitative Results

To complement the quantitative results, we provide extensive class-wise qualitative visualizations for CAAD-3K, MVTec-AD (Bergmann et al., 2019), and VisA (Zou et al., 2022). Figures 12 to 14 illustrate how CoRe-CLIP localizes anomalous evidence across contextual and structural settings, highlighting the model’s ability to identify object–scene mismatches, transfer to defect-based industrial datasets, and maintain stable localization across all categories.

*Table 13.* Per-class contextual anomaly detection results on CAAD-CC across 1-shot, 2-shot, and 4-shot settings. Reported metrics include image-level AUROC (I-AUROC), image-level AUPR, pixel-level AUROC (P-AUROC), and pixel-level PRO, providing a comprehensive view of both detection and localization performance.

Class	1-shot				2-shot				4-shot			
	I-AUROC	AUPR	P-AUROC	PRO	I-AUROC	AUPR	P-AUROC	PRO	I-AUROC	AUPR	P-AUROC	PRO
Aeroplane	79.18	79.79	97.08	81.86	93.26	90.78	96.99	83.01	65.39	61.77	96.57	82.70
Animal	79.49	82.64	98.92	93.37	86.45	83.80	97.80	85.38	99.68	99.72	99.23	93.47
Boat	94.04	94.05	97.52	85.57	85.23	90.13	97.46	86.36	96.64	97.62	98.15	87.75
Camping_tent	92.95	92.76	97.38	89.66	93.62	92.17	97.17	89.22	97.54	97.69	97.94	92.45
Car_parked	96.77	94.68	99.61	97.34	83.02	82.63	99.68	97.84	97.24	95.59	99.29	94.58
Fire	88.09	79.22	81.49	30.25	83.92	73.52	86.49	44.32	85.67	83.91	94.08	72.28
Motorbike	95.25	94.12	99.03	92.62	74.50	63.13	99.35	94.91	82.91	83.37	99.39	95.45
Person_cycling	77.53	81.61	98.06	80.97	73.61	77.83	98.28	82.51	94.72	96.74	98.21	82.25
Person_riding_horse	83.16	81.74	97.94	82.07	71.50	73.55	98.28	84.18	73.74	79.42	98.55	84.95
Person_running	88.23	91.94	99.36	87.69	68.61	78.64	99.29	87.35	98.15	98.89	99.15	83.45
Person_skateboarding	92.42	93.24	98.82	87.99	91.36	89.90	98.92	88.45	72.33	62.65	98.84	88.60
Person_with_umbrella	98.05	98.95	99.23	89.16	65.31	49.87	99.20	88.95	92.05	94.06	99.43	91.93
Shopping_cart	46.33	5.04	98.90	90.82	99.38	98.84	98.95	91.36	65.75	35.48	98.92	91.52
Sofa	92.12	89.59	97.74	89.05	99.86	99.87	98.73	93.43	99.97	99.96	99.19	94.88
Child_playing	72.04	86.24	97.27	82.65	96.39	97.22	96.48	81.70	87.81	91.28	98.63	89.09
<b>Average</b>	85.043	83.041	97.223	84.071	84.400	82.800	97.538	85.265	87.306	85.210	98.371	88.357

*Table 14.* Per-class anomaly detection performance on MVTec-AD (Bergmann et al., 2019) across 2-shot, 16-shot, 64-shot, and full-data training. Models are trained on VisA (Zou et al., 2022) with the specified number of samples and **evaluated zero-shot** on MVTec-AD (Bergmann et al., 2019), without using any MVTec-AD (Bergmann et al., 2019) training images. We report image-level AUROC (I-AUROC) and pixel-level AUROC (P-AUROC).

Class	2-shot		16-shot		64-shot		Full-shot	
	I-AUROC	P-AUROC	I-AUROC	P-AUROC	I-AUROC	P-AUROC	I-AUROC	P-AUROC
bottle	89.90	93.26	94.90	94.15	97.85	92.19	97.65	93.54
cable	72.39	80.41	82.59	80.59	86.21	87.38	80.03	87.93
capsule	79.31	94.67	88.21	94.38	92.98	91.80	92.43	93.11
carpet	99.61	99.69	99.64	99.81	99.86	99.84	99.68	99.86
grid	85.65	94.04	95.94	98.76	95.47	98.73	98.69	97.91
hazelnut	74.81	97.15	95.41	97.02	94.16	97.61	94.46	97.92
leather	100.00	99.70	100.00	99.65	99.90	99.84	100.00	99.81
metal_nut	89.99	80.92	87.62	74.50	89.60	77.93	84.62	70.65
pill	72.99	86.72	86.46	87.38	91.07	81.57	88.74	81.64
screw	83.12	98.23	86.16	98.92	89.28	98.13	88.63	98.71
tile	91.53	91.53	96.32	91.83	98.54	89.91	98.51	89.56
transistor	74.20	70.75	83.00	67.90	85.84	68.54	87.14	74.01
toothbrush	92.61	94.20	96.28	97.69	97.79	98.22	96.28	94.72
wood	98.17	98.45	99.52	98.87	99.34	98.41	99.14	98.72
zipper	79.58	94.95	95.25	97.34	95.03	97.43	94.83	97.41
Average	85.59	91.64	92.49	91.92	94.20	92.40	93.39	91.70

*Table 15.* Per-class anomaly detection performance on VisA (Zou et al., 2022) under 2-shot, 16-shot, 64-shot, and full-data training. Models are trained on MVTec-AD (Bergmann et al., 2019) with the specified number of samples and **evaluated zero-shot** on VisA (Zou et al., 2022), without using any VisA (Zou et al., 2022) training images. We report image-level AUROC (I-AUROC) and pixel-level AUROC (P-AUROC).

Class	2-shot		16-shot		64-shot		Full	
	I-AUROC	P-AUROC	I-AUROC	P-AUROC	I-AUROC	P-AUROC	I-AUROC	P-AUROC
candle	82.50	98.57	85.66	98.19	81.29	97.47	85.52	97.69
pcb3	69.03	91.89	67.63	92.99	77.28	93.14	76.14	90.87
capsules	75.75	95.37	80.91	98.55	84.54	95.62	84.49	91.90
pipe_fryum	95.07	96.02	95.57	96.58	96.03	96.54	95.05	96.15
pcb4	79.56	94.05	89.75	95.81	91.75	94.90	89.91	93.51
macaroni2	67.09	97.08	66.95	97.67	64.70	96.79	69.27	99.90
pcb2	76.27	89.23	76.14	94.62	68.16	92.79	79.20	91.03
chewinggum	99.16	99.61	96.31	99.57	97.28	99.27	95.92	99.32
macaroni1	71.83	97.54	84.51	98.05	84.01	98.16	83.68	98.00
cashew	85.88	92.42	91.34	94.87	92.53	93.14	92.15	94.53
fryum	87.27	94.39	90.29	93.88	93.22	95.84	94.49	95.49
pcb1	86.76	87.80	82.92	92.54	82.01	91.14	73.03	91.05
Average	81.35	94.50	84.00	95.50	84.40	95.40	84.90	95.50

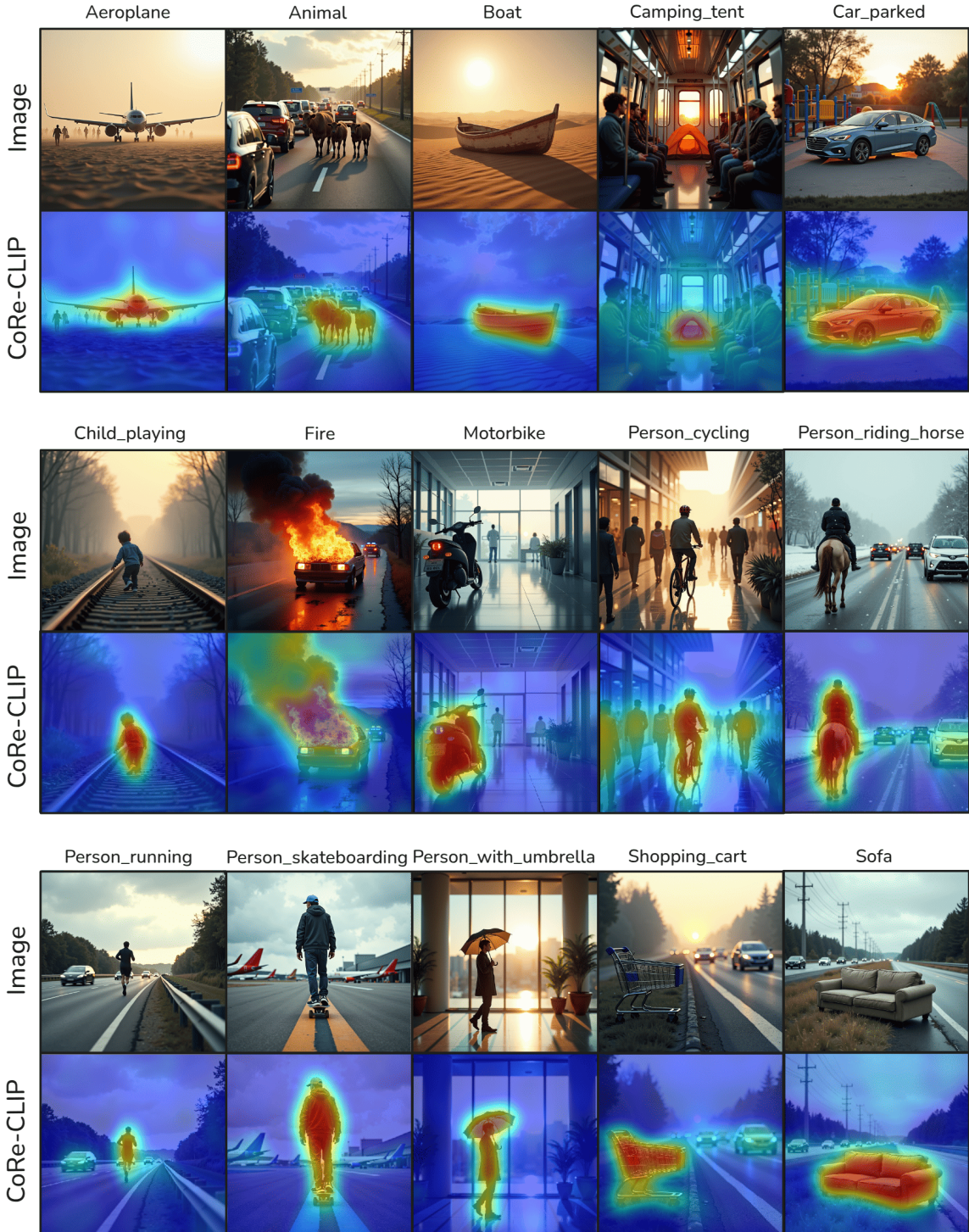


Figure 12. Class-wise anomaly localization on CAAD-3K. For each anomalous image, the heatmaps show CoRe-CLIP’s pixel-level anomaly attribution. The model consistently isolates the region corresponding to the object–scene incompatibility, demonstrating precise contextual reasoning across 15 categories.

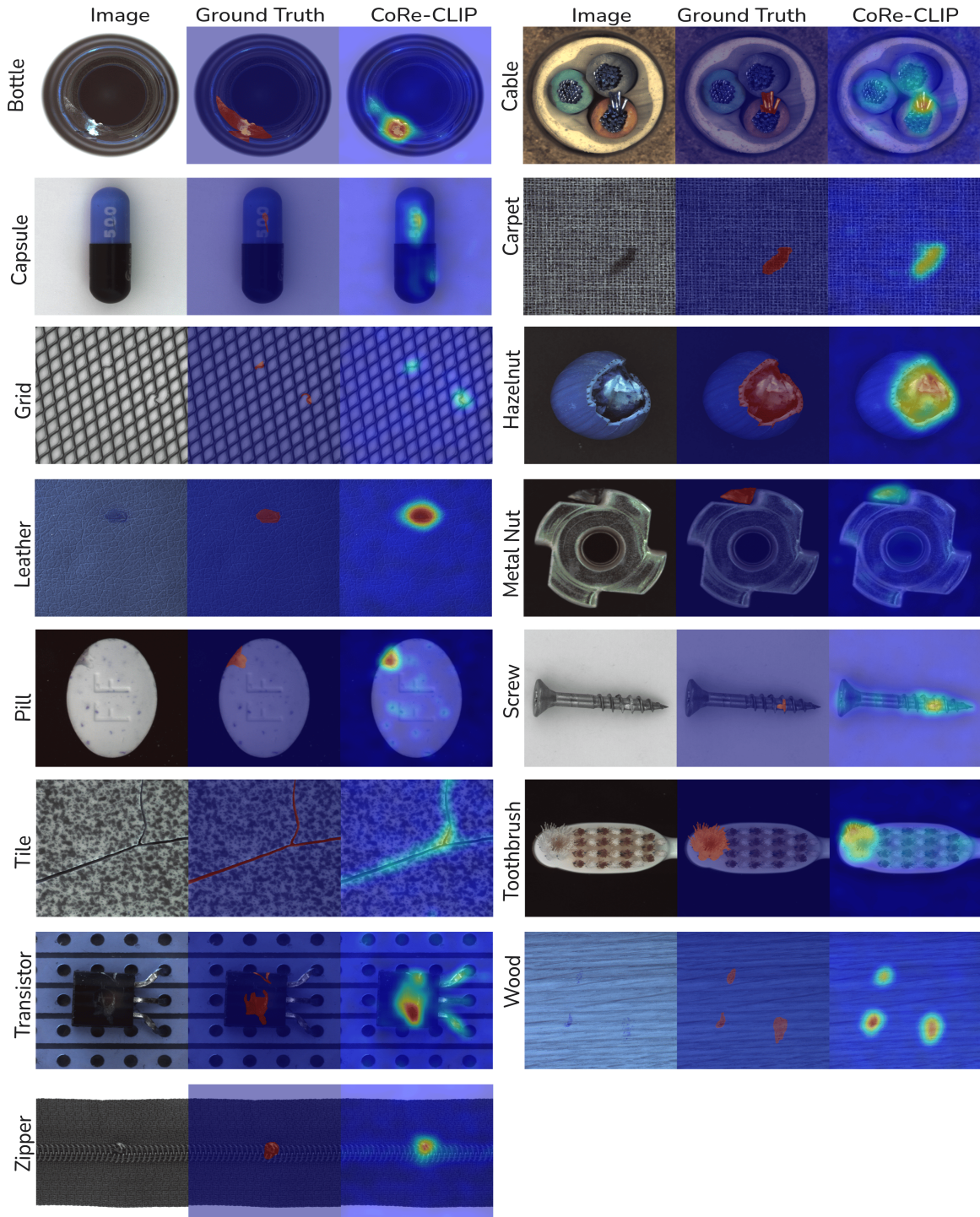


Figure 13. Zero-shot qualitative results on MVTec-AD (Bergmann et al., 2019). CoRe-CLIP is trained on VisA (Zou et al., 2022) and evaluated on MVTec-AD (Bergmann et al., 2019). In this zero-shot transfer setting, CoRe-CLIP yields precise structural defect maps despite receiving no supervision from MVTec-AD (Bergmann et al., 2019), confirming that the model’s context-aware design does not compromise its ability to generalize to purely structural anomalies.

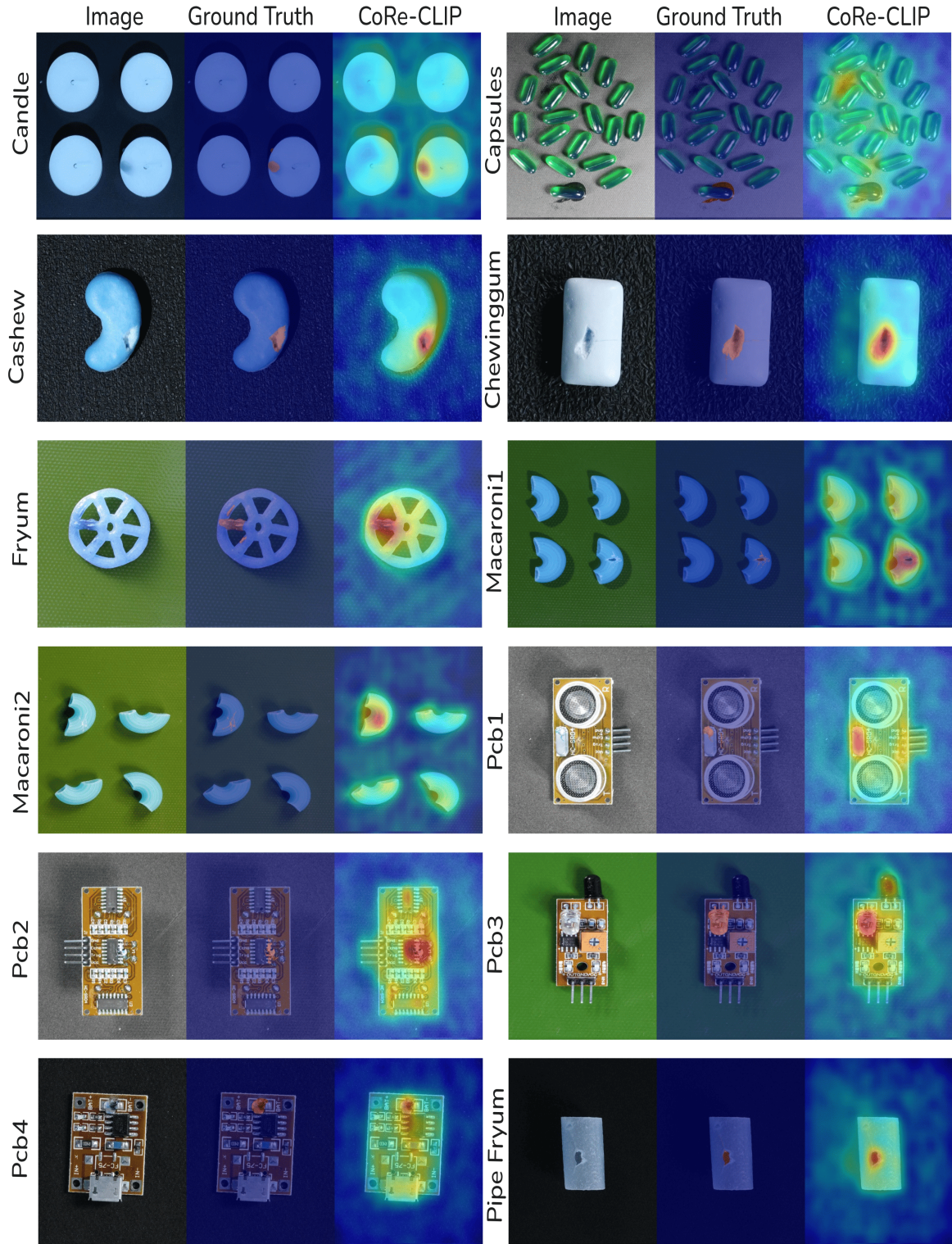


Figure 14. Zero-shot qualitative results on **VisA** (Zou et al., 2022). CoRe-CLIP is trained on **MVTec-AD** (Bergmann et al., 2019) and evaluated on **VisA** (Zou et al., 2022) without any access to **VisA** (Zou et al., 2022) anomaly images. The model accurately highlights defect regions across diverse objects and illumination conditions, confirming its robust cross-dataset generalization and its ability to localize structural anomalies even when trained on a different anomaly dataset.